Deep JHK_s and *Spitzer* Imaging of Four Isolated Molecular Cloud Cores

Nicholas L. Chapman[1,2], Lee G. Mundy[1]

ABSTRACT

We present observations in eight wavebands from $1.25 - 24\,\mu$m of four dense cores: L204C-2, L1152, L1155C-2, and L1228. Our goals are to study the YSO population of these cores and to measure the mid-infrared extinction law. With our combined near-infrared and *Spitzer* photometry, we classify each source in the cores as, among other things, background stars, galaxies, or embedded young stellar objects (YSOs). L1152 contains three YSOs and L1228 has seven, but neither L204C-2 nor L1155C-2 appear to contain any YSOs. We estimate an upper limit of 7×10^{-5} to 5×10^{-4} $L_\odot$ for any undiscovered YSOs in our cores. We also compute the line-of-sight extinction law towards each background star. These measurements are averaged spatially, to create χ^2 maps of the changes in the mid-infrared extinction law throughout our cores, and also in different ranges of extinction. From the χ^2 maps we identify two small regions in L1152 and L1228 where the outflows in those cores appear to be destroying the larger dust grains, thus altering the extinction law in those regions. On average, however, our extinction law is relatively flat from 3.6 to 24 μm for all ranges of extinction and in all four cores. From 3.6 to 8 μm this law is consistent with a dust model that includes larger dust grains than the diffuse interstellar medium, which suggests grain growth has occurred in our cores. At 24 μm, our extinction law is $2 - 4\times$ higher than predicted by dust models. However, it is similar to other empirical measurements.

Subject headings: dust, extinction—ISM: globules—stars: formation

1. Introduction

In the standard model of low-mass star formation, dense cores are the precursors of star formation (Shu et al. 1987). Therefore, to understand the process of star formation,

[1]Department of Astronomy, University of Maryland, College Park, MD 20742; chapman@astro.umd.edu

[2]Jet Propulsion Laboratory, California Institute of Technology, 4800 Oak Grove Drive, MS 301-429, Pasadena, CA 91109

one needs to observe the physical conditions of these cores. Embedded young stellar objects (YSOs) are sometimes detected in these cores. These YSOs are partially obscured by the dust within the cores. To accurately model their physical properties requires knowledge of the quantity of dust and its composition, since both affect the degree of attenuation, or extinction, of starlight. By studying the dust, one can learn about its chemistry and evolution. Furthermore, the dust provides a direct measure of the column density and mass. Molecular tracers can suffer depletion in dense regions, making mass estimates from them unreliable.

In this paper we use *Spitzer* and deep ground-based JHK_s observations to probe the dust properties within four cores: L204C-2, L1152, L1155C-2, and L1228. Two of our cores, L1152 and L1228, have known protostars while the other two do not. Our first goal in this paper is to examine the YSO population of these cores and to look for faint previously unknown protostars in all four cores. Second, we will compute the extinction law in each core and compare it to the predictions of three dust models to draw conclusions about the dust properties within the cores. This paper is organized as follows: § 2 describes our observations and data processing pipeline including source classification, the removal of misidentified background galaxies, and how we computed line-of-sight (LOS) extinctions to each star. In § 3 we use these LOS extinctions to create extinction maps for each core. Then, § 4 explores the YSO content in our cores. In § 5 we compute the relative extinction as a function of wavelength, the extinction law, for each core. We also create maps of the χ^2 maps of the difference between the observed and predicted extinction laws and compare to the extinction maps. Finally, we summarize our results in § 6.

2. Observations

Table 1 lists the location and our assumed distance to each of our cores: L204C-2, L1152, L1155C-2, and L1228. These cores were all observed as part of the *Spitzer* Legacy Science program "From Molecular Cores to Planet-forming Disks" (c2d) (Evans et al. 2003). Using *Spitzer*, we re-observed these cores with $\sim 10\times$ the integration time as c2d to look for faint protostars in the cores. These observations were part of GO program #3656. We observed each core in two epochs, where the second epoch was separated from the first by as little as one day but could be up to almost a month later. L204C-2 is located at an ecliptic latitude where asteroids may be a problem; the separation of the two observing epochs ensures we can identify these sources. IRAC ($3.6 - 8\,\mu$m) and MIPS1 ($24\,\mu$m) were observed separately, resulting in four *Spitzer* Astronomical Observation Requests (AORs) per core. Our *Spitzer* AORs are listed in Table 2.

To complement our *Spitzer* data, we obtained deep JHK_s data using the FLoridA Multi-object Imaging Near-ir Grism Observational Spectrometer (FLAMINGOS) (Elston 1998) instrument installed on the 4-meter telescope at Kitt Peak. These JHK_s observations spanned four epochs from October 2003 to June 2006. The FLAMINGOS field-of-view is $\sim 11' \times 11'$. Each field consisted of multiple dithers with small offsets around a central position. The total integration time per pixel was 12 minutes (J), 6 minutes (H), and 3 minutes (K_s). For two fields each in L1152 and L1155C-2 (centered on the core) we took even deeper observations with total integration times of $\sim$ 1 hour (J), $\sim$ 1 hour (H) and $\sim$ 45 minutes (K_s). Except for a small corner in L204C-2, the JHK_s data completely cover the areas mapped with *Spitzer*. In Figures 1-4 we show three-color images of each core and also selected subregions.

2.1. Data Reduction

We reduced our JHK_s data using python and PyRAF. Each FLAMINGOS field consisted of multiple dithers with small offsets around a central position. To create our science images, we first subtracted a median filtered dark image from each dither. Second, the dithers were flat-fielded by dividing out a dome flat. Next, we subtracted off the sky. This is critical for IR observations where the sky is typically much brighter than the astronomical objects of interest. We used a two-pass sky subtraction with a running median: stars were identified from the first pass, then masked out in the second pass to produce an improved sky subtraction. Finally, we averaged together the individual dithers for each field.

We used the 2MASS catalog to correct the coordinates in each field and also to calibrate the photometry. The stars in each field were found using the IRAF task `daofind` and we used `daophot` to compute their point spread function (PSF) photometry. We visually inspected the results to remove false sources identified by `daofind` and also to add sources missed by the source extractor. Finally, we bandmerged the individual J, H, and K_s detections into a single JHK_s catalog for each core.

Our *Spitzer* data were processed through the standard c2d pipeline. For a full description of this pipeline, please refer to the c2d data delivery documentation available on the Spitzer Science Center's (SSC) website[1]. We will summarize the pipeline here. We started with the Basic Calibrated Datasets (BCDs) processed by the SSC using their S13 pipeline. We then corrected several image artifacts caused by bright sources and cosmic rays and also some instrumental effects. Lastly, we applied location-dependent photometric corrections

[1] `http://ssc.spitzer.caltech.edu/legacy/c2dhistory.html`

that account for variations in the detector response across the array.

After improving the BCDs we combined them into mosaics for each core using the SSC's software MOPEX (Makovoz & Marleau 2005). We then extracted sources using a modified version of DoPHOT (Schechter et al. 1993). DoPHOT fits PSFs and as sources are found they are subtracted from the images. Next, we bandmerged the individual detections from the 3.6 to 24 μm wavebands and attempted to determine upper limits for non-detections. Since we did not obtain any short integration "high dynamic range" (HDR) observations, we used the c2d observations that *do* contain HDR frames to correct for saturated fluxes. We compared our fluxes with the c2d fluxes in each IRAC band and empirically determined a flux limit at which our values systematically diverged from c2d's. We then substituted the c2d fluxes for any sources with a c2d flux brighter than this limit. These limits were: 35, 35, 300, and 150 mJy for the 3.6, 4.5, 5.8, and 8.0 μm bands, respectively.

Finally, we combined our 3.6 to 24 μm and deep JHK_s catalogs to create bandmerged catalogs from 1.25 to 24 μm for each of the four cores.

2.2. Data Quality

The mean difference in position between sources in our JHK_s catalogs and in the 2MASS catalogs is $0\farcs15$, and 95% of our sources have a difference in position of $\leq 0\farcs6$ (around 2 pixels on the FLAMINGOS CCD). We also computed the flux difference between our Kitt Peak observations and the 2MASS catalog. The resultant distributions are gaussian with mean $\lesssim 0.01$ mJy and $\sigma = 4 - 5\%$ in all three of the JHK_s bands.

Even though our *Spitzer* data are not part of the c2d program, we processed them through the c2d pipeline so we expect the errors in the *Spitzer* wavebands will be similar to c2d's. The c2d delivery documentation discusses three sources of uncertainty: statistical, systematic, and absolute. The first two of these are incorporated into the photometric uncertainties listed in the c2d catalog. These errors are derived from the repeatability of flux measurements using the c2d pipeline. The c2d documentation lists a 4.6% systematic error for IRAC and 9.2% for MIPS. Combining the systematic and statistical errors, our final photometric uncertainties are approximately 5% in IRAC and 10% in MIPS. The absolute uncertainties in the flux calibration are 1.5% and 4%, respectively, for the IRAC and MIPS1 (24 μm) bands. We obtained these values from the Infrared Array Camera (IRAC) Data Handbook, Version 3.0 and the Multiband Imaging Photometer for Spitzer (MIPS) Data Handbook, version 3.3.0. The absolute uncertainties are added in quadrature with the photometric errors during source classification, but are not used elsewhere since they are

smaller than the photometric errors.

Table 3 lists our 10σ and 5σ limits for each wavelength. Our 10σ JHK_s limits are ~ 3.5 magnitudes deeper than the 2MASS limits of 15.8, 15.1, and 14.3 magnitudes, respectively. In the dense core regions of L1152 and L1155C-2 we were able to take even deeper JHK_s observations. These limits are listed in parentheses in the table. As for the *Spitzer* wavebands, our 10σ limits are 1.5-2 magnitudes fainter in the IRAC bands and 2.5 magnitudes fainter in the MIPS1 band compared to c2d.

2.3. Extinction and Star Classification

We used a modified version of the c2d data pipeline to classify sources based on their spectral energy distribution (SED) from 1.25 to 24 μm. The standard c2d pipeline uses all available wavelengths to compute the extinction towards each star:

$$\log(F_{obs}(\lambda)/F_{model}(\lambda)) = \log(k) - 0.4 \times C_{ext}(\lambda) \times A_V \quad (1)$$

where $F_{model}(\lambda)$ is the stellar photosphere model, k is the scaling factor of the model for a particular star, and $C_{ext}(\lambda) \equiv A_\lambda/A_V$ is the ratio of the extinction at wavelength λ to visual extinction from the dust extinction law. k and A_V can be derived from the linear χ^2 fit of this equation by adopting stellar photosphere and dust extinction models. The stellar models used are based on the Kurucz-Lejeune models and come from the SSC's online "Star-Pet" tool[2]. For the 2MASS bands, the observed $J-H$ and $H-K$ colors of stars (Koornneef 1983) were translated to fluxes relative to K band and the difference between the K and K_s bands was ignored.

Sources fit by Equation 1 with a goodness-of-fit $q \geq 0.1$ were classified as reddened stars, while those that did not fit were compared with other templates to classify them. The goodness-of-fit, q, is the incomplete gamma function and gives the probability that the statistical χ^2 distribution would exceed our observed χ^2 (computed from Eq. 1) by chance. Thus, a very small q means it is unlikely that the differences between our data and a given F_{model} are due to chance, i.e. the model is unlikely to be an accurate fit to the data (Press et al. 1992). Our minimum q value of 0.1 is the same one used by the c2d team for identifying stars.

We slightly modified this procedure for this paper. First, the extinction is computed

[2]`http://ssc.spitzer.caltech.edu/tools/starpet`

for each source using the JHK_s bands and the NICER technique (Lombardi & Alves 2001). The NICER technique relies on the assumption of intrinsic values for the $J-H$ and $H-K_s$ colors of stars. For this paper we adopted the values $J-H^{intrinsic} = 0.50 \pm 0.12$ and $H-K_s{}^{intrinsic} = 0.18 \pm 0.04$. These values were derived from the average stellar model computed in Appendix A. Then, using Equation 1, we identified the stars with the extinction held fixed. We also computed extinctions in A_{K_s} rather than the more traditional A_V so we can directly compare our results with those of other authors.

We made this change because one of our goals in this paper is to compute the extinction law at the IRAC and MIPS wavelengths. The method we use for deriving the mid-infrared extinction law (A_λ/A_{K_s}) is dependent on A_{K_s} so we cannot use these wavelengths when computing A_{K_s}. However, we still need to choose an appropriate extinction law. This will be used to compute A_{K_s} from the JHK_s bands and also for the source classification. We considered two dust models, the Weingartner & Draine (2001) $R_V = 3.1$ and $R_V = 5.5$ models. The $R_V = 3.1$ model (hereafter WD3.1) is designed to reproduce the extinction law of the diffuse interstellar medium; the $R_V = 5.5$ model (hereafter WD5.5) fits the observed law of denser regions. We found in Chapman et al. (2009) (hereafter Paper I) that some heavily extincted stars may only fit the WD5.5 dust model rather than the more traditional WD3.1 extinction law. In lower extinction regions both models tend to fit equally well. Therefore, for source classification we have chosen to use the WD5.5 dust model.

2.4. High Reliability Star Catalogs

The c2d data pipeline classifies sources according to their SED and infrared colors. Among other classifications, sources are identified as stars, 'Galaxy candidates' (Galc), or 'Young Stellar Object candidates' (YSOc). With YSOc, Galc, and other infrared excess sources we cannot separate out the expected flux of the SED from changes in those fluxes due to variations in the extinction law. Therefore, we want to concentrate on those sources classified as stars for studying the variations in the extinction law.

To create our high-reliability star catalogs we first selected all sources classified as stars, excluding those classified as stars when one waveband was dropped because we did not want a prominent absorption or emission line to bias our results. Furthermore, because accurate extinctions are essential to our analysis, we required sources to have detections $\geq 7\sigma$ in each of the JHK_s bands. Lastly, we removed suspected faint background galaxies from our star catalogs using the criteria listed in § 2.5.

The number of stars in our high-reliability catalogs is: 3,244 (L204C-2), 4,038 (L1152),

3,926 (L1155C-2), and 1,850 (L1228). We then removed a few sources, as described below, to obtain our final catalogs. The percentage of sources removed is $< 1\%$ for L204C-2, L1152, and L1155C-2, and 2.2% in L1228.

2.5. Misidentified Background Galaxies

Although we carefully selected only the most reliable stars to construct our catalogs, it appears that some faint background galaxies are misidentified as stars. This can be readily seen in Figure 5, where we plot $J - H$ versus $H - K_s$ for the stars in our cores. The stars brighter than 15th magnitudes at K_s (black points) follow the reddening vector, while many of the fainter sources (gray crosses) do not. The 'known' stars and background galaxies are shown as white and dark gray circles, respectively. Our method for creating these two populations of sources is described below. Most of the 'known' background galaxies are grouped to the right of the bright sources, in the same area as those gray crosses which do not follow the reddening vector. This suggests that these gray crosses are actually background galaxies. Foster et al. (2008), using near-infrared data from Perseus, also concluded that sources in this approximate region of a $J-H$ versus $H-K_s$ color-color diagram are likely to be background galaxies. Background galaxies are not the only explanation for these sources. It is possible that a few of them may be YSOs. In § 4.3 we will discuss the prospects for faint YSOs in the cores.

To create samples of 'known' stars and background galaxies, we could not start from the high-reliability catalogs since those explicitly exclude non-star objects. Instead, we began with the full catalogs and imposed the same 7σ cutoff in the JHK_s bands as we did for the high-reliability star catalogs. Second, we selected only those sources with 24 μm detections $\geq 3\sigma$. The resultant sources are plotted in Figure 6. We used different symbols depending on how sources were classified in § 2.3: stars are shown as circles, Galc sources are squares, YSOc's are shown as triangles, and plus signs for everything else. Furthermore, the shaded contours are the c2d processed SWIRE data of region ELAIS N1 (Surace et al. 2004). Since the ELAIS N1 region is near the north Galactic pole, it should contain nothing but stars and background galaxies making it useful for comparison. From this figure, we selected 'known' populations of stars and background galaxies. The stars are those sources with $K_s - [24] \leq 1$ and the background galaxies have $K_s \geq 15$ and $K_s - [24] \geq 4$.

We will follow a procedure similar to that in Paper I to eliminate the misidentified background galaxies from our high-reliability star catalogs. First, we select suspected background galaxies with the following colors: $J - H \geq 0.6$, $H - K_s \geq 0.6$, and $J - H \leq 1.9 \times (H - K_s) - 0.16$. These selections are shown as dashed lines in Figure 5. Then, just

using the sources selected by these colors, we plotted them on two color-color diagrams in Figure 7 along with our 'known' star and background galaxy samples. There is a clear separation between the 'known' stars and background galaxies. The dashed line in the figure is: $H - K_s = 1.32x$, where x is either $K_s - [3.6]$ or $K_s - [4.5]$. We combine these two selections to remove our misidentified background galaxies. These selection criteria are the same empirically derived ones used in Paper I, but with one important difference: because there is such a large degree of non-overlap spatially between the four IRAC bands, we relaxed the second criterion from Paper I so that sources only need to satisfy either the first half or the second half of it. Our criteria are:

1. $J - H \geq 0.6$, $H - K_s \geq 0.6$, and $J - H \leq 1.9 \times (H - K_s) - 0.16$
2. $H - K_s \leq 1.32 \times (K_s - [3.6])$ or $H - K_s \leq 1.32 \times (K_s - [4.5])$

Sources satisfying both criteria were removed from our catalogs. After removal of these sources, The number of stars in our final high-reliability catalogs is: 3,219 (L204C-2), 4,010 (L1152), 3,891 (L1155C-2), and 1,810 (L1228).

3. Extinction Maps

Our star catalogs contain a line-of-sight extinction measurement to each star calculated using the NICER technique (Lombardi & Alves 2001) and the WD5.5 dust model. We converted these randomly distributed samplings of the true extinction within each core into uniformly sampled maps by overlaying a grid on each core with an 18″ spacing between grid elements. At each grid position, an extinction value was computed as the average of the individual measurements within a 90″ radius. This average is weighted both by the uncertainty of each line-of-sight extinction value and also by a gaussian function with full width half maximum (FWHM) equal to 90″. Thus, our final maps have 90″ resolution with 5 pixels across the FWHM. By setting our integration radius to equal the FWHM (2.3548σ), we capture 98.14% of the total area of the gaussian weighting function, and avoid the unrealistic scenario of utilizing extinction values from arbitrarily large distances away from each grid position.

We subtracted foreground stars in a simple way: For each cell with more than 2 stars, we computed the mean and median A_{K_s} values. If these two statistics differed by $> 25\%$, then we dropped the source with the lowest A_{K_s} and recomputed the mean. If the difference between the old and new mean is less than 25%, we re-added the dropped source to our catalog. After identifying all sources to drop, we recomputed the extinctions in every cell.

Despite its simpleness, we found this procedure to be very effective in removing foreground stars. The 25% cutoff was empirically chosen after we ran some tests with different cutoff parameters.

We chose the 90″ resolution because this gave us a reasonable number of stars per cell for good statistics. The median number of stars per cell is $\sim 35 - 40$ for L204C-2, L1152, and L1155C-2, and 18 in L1228. The percentage of cells with ≤ 5 stars is 6% in L1152 and L1155C-2, 11% in L204C-2, and 14% in L1228. Figures 8 - 11 are extinction maps of our four cores. The contours in each map start at $A_{K_s} = 0.5$ mag in steps of 0.15 (3σ). We also plotted the YSOc and Galc sources from our catalogs on the extinction maps and numbered the YSOs from § 4. Lastly, because YSOc and Galc sources can be classified only in regions with IRAC1 through IRAC4 and MIPS1, we outlined the area in each core where all these bands overlap.

The core of L204C-2 has a peak extinction of $A_{K_s} = 2.1$. Extending northward from the central core is a dust filament with two other lower density extinction peaks. West of the core is a low density clump with a peak extinction of $A_{K_s} = 0.8$. We detect no YSOs in L204C-2. One Galc object is located near the center of the core, however, as we will discuss in § 4 this source has an SED consistent with a heavily extincted background star.

L1152 is a small core with peak $A_{K_s} = 1.8$. To the east are two additional separate extinction peaks. Both of these have a lower column density than the main core. A bright YSOc is embedded in the primary core, slightly northeast of the extinction peak. One lobe of an outflow can be seen in J through IRAC4 extending southwest from this YSO. The other two YSOs are northeast of the core, and slightly offset from the northernmost extinction peak.

L1155C-2 is an extended core with two extinction peaks, the northernmost has a higher peak extinction of 1.7 magnitudes. A dust filament that is part of L1155E appears in the southern third of the map. Like L204C-2, this core also appears starless.

The central core of L1228 contains two extinction peaks and appears pinched in the middle. The peak extinction in this core is 2.2 magnitudes. This pinching may simply be an artifact caused by the lower median number of stars per cell compared with the other cores or it may indicate clearing by the outflow since the pinch direction lines up with the east-west outflow seen in Figure 4. Several other extinction peaks are nearby, mostly north of the core. L1228 has previously been classified as a starred core, and several YSOs are identified in the core; most have not been previously identified. Despite having similar Galactic coordinates as L1152 and L1155C-2, only two Galc objects appear in this core. This is because L1152 and L1155C-2 have deeper JHK_s data than L1228, therefore many more Galc objects fall

into our high-reliability catalogs for those cores than in L1228.

4. Young Stellar Objects

Ten sources are classified as YSOc in our cores. However, a source can be classified as a YSOc only if it is detected in all *Spitzer* wavebands from 3.6 to 24 μm. This is because various empirically derived *Spitzer* colors and magnitudes are used in classifying YSOc sources (Harvey et al. 2007). Therefore, to our initial list of 10 sources we added six potential YSOs that were not classified as YSOc. First, we included sources from Figure 6 with $K_s - [24] \geq 3$ and $K_s \leq 14.5$. Most of the sources in this region are classified as YSOs already. This selection added two sources in L1228, neither of which is classified as YSOc because they are outside of the area observed in IRAC2 and IRAC4 (4.5 and 8 μm). It is also possible that faint YSOs may be misidentified as Galc. Therefore, we also selected four Galc objects from Figures 8-11 that were located near the dense cores; one source each in L204C-2 and L1152 and two in L1228. This brought our total number of possible YSOs to 16.

After we visually inspected all 16 sources, we excluded the Galc objects in L1152 and L1228 since all were visually extended in mosaics, meaning they are likely to be true background galaxies. We also excluded the one Galc object from L204C-2 because this source has the SED of a heavily extincted star. In Figure 6, this source is the Galc at $K_s - [24] = 1.5$. Furthermore, we excluded one of the YSOc objects in L1228 that is clearly a knot of emission from the outflow and not a real source. Lastly, we also excluded one of the non-YSOc sources in L1228 that only has an infrared excess at 24 μm. The 24 μm flux for this source appears confused with two other nearby sources detected at shorter wavelengths. We are left with 10 YSOs, three in L1152 and seven in L1228. Note that now we are identifying these sources as Young Stellar Objects and not Young Stellar Object candidates. In Table 4 we list the fluxes and positions of these 10 YSOs present in our cores. For each YSO, we added the 70 μm flux from c2d, if detected. Neither L204C-2 nor L1155C-2 appear to contain any YSOs. In § 4.3 we will place some upper limits on unidentified YSOs in our cores.

We modeled the SED for our 10 YSOs using an online tool (Robitaille et al. 2007). This tool fits an input SED to a pre-computed grid of YSO models. In Figure 12 we show all models with $\chi^2 \leq 2 \times \chi^2_{best}$, where χ^2_{best} is the χ^2 for the best-fitting model. The best-fit model for each YSO is shown in black with other models shown in gray. Each model has numerous parameters, a few of which we have listed in Table 5. We show the range of values for envelope accretion rate, disk mass, interstellar extinction (A_V), and bolometric luminosity plus the average value for each quantity. Note that the Robitaille models do include stellar masses, however these are not constrained for embedded objects, so we will not use them

here (Robitaille, private communication).

We also classified our YSOs based on their value of $\alpha = d \log \lambda F_\lambda / d \log \lambda$, the best-fit slope of a straight line to the SED from K_s to 24 μm. We then separated the YSOs into one of four classes using the method of Greene et al. (1994). Following an evolutionary sequence from youngest to oldest YSO, they are: Class I ($\alpha \geq 0.3$); Flat spectrum ($0.3 > \alpha \geq -0.3$); Class II ($-0.3 > \alpha \geq -1.6$); and Class III ($\alpha < -1.6$). We have included sources with $\alpha = 0.3$ in Class I since these were undefined by Greene et al. (1994). Our YSOs are a mixture of Class I, Flat spectrum, and Class II sources, but no Class III objects. This suggests that the YSO population in these cores is relatively young.

4.1. L1152 YSOs

Two of the three YSOs in L1152, IRAS 20353+6742 and IRAS 20359+6745, are previously known and both have outflows associated with them. IRAS 20353+6742 is the source embedded in the L1152 core and is source #1 in Tables 4 and 5. Only one lobe of the outflow is visible, but it can be seen from J through IRAC4 (Figure 2). The second known source, IRAS 20359+6745, is source #3 in Tables 4 and 5. This YSO has an outflow associated with it that is visible in JHK_s but not at longer wavelengths. The Herbig-Haro object HH376A is located 2.′6 to the southwest. The bowshock shape of HH376A and its location along the apparent axis of the JHK_s outflow from source #3 suggests it may be part of the same system. We show both of these features in Figure 2. The remaining YSO is approximately 1′ to the west of IRAS 20359+6745. We found no references to this source in SIMBAD[3].

4.2. L1228 YSOs

We identified seven YSOs in L1228. Six of these are classified as YSOc based on their colors while the remaining one cannot be classified as such because it appears outside of the area covered by IRAC2 and IRAC4. Five of the YSOc sources appear to be spatially coincident with the core of L1228. The brightest source is #7 and is identified as IRAS 20582+7724. This is the only previously known YSO in the core of L1228. It appears to be the driving source for a CO outflow, HH 199 (Haikala & Laureijs 1989; Bally et al. 1995). The axis of the CO outflow is about 40° different from the east-west axis formed by the infrared knots. Bally et al. (1995) conclude this is likely due to precession of the jet that

[3]http://simbad.u-strasbg.fr/simbad/

drives the outflow. In Figure 4 the green dashed line shows the axis of the infrared knots while the red dashed line shows the axis of the CO outflow.

Sources #5 and #6 are located about 1.′2 northwest of IRAS 20582+7724 and separated from each other by 5.″3. Because of this separation, they are not resolved at 70 μm ($FWHM = 17''$) and not fully resolved at 24 μm ($FWHM = 5.''7$). Even though we were able to extract a flux at 24 μm for both sources, we suspect that the 24 μm flux for source #6 is artificially high. When fitting YSO models, we found that excluding this datapoint decreased χ^2_{best} from 174 to 48, the latter is more in line with the χ^2_{best} for the other sources. Therefore, we excluded this datapoint for the models listed in Table 5 and shown in Figure 12. It is also possible that the 70 μm flux for source #5 includes some contribution from source #6 as well. Bally et al. (1995) detected a series of infrared emission knots that form the HH 200 outflow which has its origin at the position of sources #5 and #6. It is unknown which of these is the driving source of the outflow. We show the approximate axis of this outflow as a yellow dashed line in Figure 4. There is some outflow emission immediately to the northeast of sources #5 and #6 which lies along the outflow axis.

Lastly, the two YSOs not spatially coincident with the L1228 core are sources #4 and #10. Source #10 does not meet the criteria for YSOc because it is lacking IRAC2 and IRAC4 fluxes.

4.3. Constraints On New Faint YSOs

We did not detect any YSOc sources that were not already detected by c2d. The converse is also true, in the c2d catalogs of all four cores, there is only one YSOc object not in our catalogs. However, after inspection we determined this object to be another emission knot from the east-west outflow. This lack of additional YSOc sources is not too surprising since the YSOc selection criteria were tuned to the sensitivity of the c2d-processed SWIRE data. Therefore, any sources fainter than those limits are likely to be automatically classified as Galc. It was for this reason that we also considered some Galc sources when compiling our YSO catalog. However, from Figures 1-4 it is clear that there are many bright 24 μm sources in our cores, far more than the number of YSOc and Galc objects.

We would like to use these objects to place limits on possible faint YSOs in these cores. If we select sources from the overlap region of all five bands with 24 μm detections $\geq 3\sigma$, then exclude any star or YSOc sources and also any Galc sources in Figure 6, we are left with 634 sources in all four cores. These 634 sources have a median 24 μm flux of 0.21 mJy (11.3 magnitude). Just 47 of them are detected at K_s, but these have a median flux of 0.04 mJy

(18.1 magnitude). Our 5σ detection limit for K_s is 18.4 magnitudes, or 19.3 magnitudes for the deep observations. If we assume that the remaining sources must be fainter than these limits in order to be undetected at K_s, that means they must have $K_s - [24] \gtrsim 7 - 8$. From Figure 6, the boundary between Flat/Class I is at $K_s - [24] = 8.31$. Therefore, we expect any new YSOs existing among these 634 sources to be fainter than 18-19 magnitudes at K_s and to be very young Flat/Class I objects.

To put an upper limit on the luminosity of any embedded YSOs, we integrated our median SED assuming a blackbody extrapolation shortward of J band and longward of 24 μm. The temperature of the blackbody was derived from the flux ratio of the first two and last two wavelengths, for the shortward and longward extrapolations, respectively. The luminosity ranges from 7×10^{-5} $L_\odot$ for L204C-2 (the closest core) to 5×10^{-4} $L_\odot$ for the two furthest cores (L1152 and L1155C-2).

Are any of these sources YSOs? To answer this question is beyond the scope of this paper. However, given that the sources are distributed throughout the observed regions, it is very likely that most, if not all, are background galaxies. Spectra of individual sources would be needed to identify any YSOs hidden among the galaxies.

5. Dust Properties

The dust properties affect the extinction law. So, to study the dust properties, we will compute the extinction law. By using the extinctions computed from the JHK_s bands we can extrapolate the extinction law in the *Spitzer* wavebands. Starting from Equation 1, but using A_{K_s} instead of A_V, we re-arrange it to solve for C_{ext}, defined as A_λ/A_{K_s}:

$$C_{ext}(\lambda) = \frac{2.5}{A_{K_s}}[\log(k) - \log(F_{obs}(\lambda)/F_{model}(\lambda))] \tag{2}$$

Since we are only interested in *differences* in the extinction law, we can subtract $C_{ext}(K_s)$ to eliminate the need for k, the scaling factor. Furthermore, because $C_{ext}(K_s) \equiv 1$ and $F_{model}(K_s) \equiv 1$ (all stellar models are scaled relative to K_s), the equation simplifies to:

$$C_{ext}(\lambda) = \frac{2.5}{A_{K_s}}\left[\log(F_{obs}(K_s)/F_{obs}(\lambda)) + \log F_{model}(\lambda)\right] + 1 \tag{3}$$

For F_{model} we will use the average stellar model derived in Appendix A.

5.1. Spatial Dependence of the Extinction Law

In this section we will create a two-dimensional map of how the extinction law changes in each core. We start by defining a reduced χ^2 for each star:

$$\chi^2 = \frac{1}{n-1} \sum_{\lambda}^{n} \left(\frac{C_{ext}^{obs}(\lambda) - C_{ext}^{model}(\lambda)}{\sigma_\lambda} \right)^2 \tag{4}$$

where $C_{ext}^{obs}(\lambda)$ is computed from Equation 3, C_{ext}^{model} is the extinction law for a given dust model, and σ_λ is the uncertainty in C_{ext}^{obs}. We sum only over the IRAC bands because, as we will see, the extinction law at 24 μm does not fit any current dust models and therefore we excluded this wavelength to avoid biasing our χ^2. Furthermore, we excluded any negative values for A_λ/A_{K_s} as unphysical. We will discuss the biases introduced by this assumption in § 5.3. We will refer to this reduced χ^2 as "χ^2" in this paper.

Using Equation 4 we computed the line-of-sight χ^2 value for each star. Then, to convert our line-of-sight measurements into a map, we followed the same procedure as we did when creating our A_{K_s} maps. In Figures 13 - 16 we show maps of the extinction and χ^2 calculated using both the WD3.1 and WD5.5 dust models. The χ^2 maps have the same resolution as the extinction maps, 90″. Our contours start at $\chi^2 = 4$ because we observe a definite transition between the WD3.1 and WD5.5 dust models at this approximate χ^2 value (see Figure 17). Statistically, a $\chi^2 = 4$ would arise by chance about 5% of the time.

The correspondence between the extinction, A_{K_s}, and the $R_V = 3.1$ χ^2 maps is quite remarkable. In all of our cores, the overall shape and the extinction peaks are mirrored in the WD3.1 χ^2 map. Many of the extinction features not associated with the cores also appear in the χ^2 map such as the dusty filament to the north of L204C-2, the two separate extinction peaks in L1152, and much of the structure in L1228.

To make a quantitative comparison between χ^2 and A_{K_s}, we binned our data in A_{K_s} and for each bin determined the average χ^2 with both the WD3.1 and WD5.5 models. Our results are shown in Figure 17. $R_V = 3.1$ χ^2 is shown in black while $R_V = 5.5$ is shown in gray. At low extinction, $A_{K_s} \lesssim 0.6$, the $R_V = 3.1$ and $R_V = 5.5$ χ^2 are very similar to each other, suggesting that at low extinctions it is difficult to distinguish between these two models with our technique. Above $A_{K_s} \sim 0.6$ the $R_V = 3.1$ χ^2 rises sharply while the $R_V = 5.5$ χ^2 stays roughly constant or increases only slightly.

The observed behavior in our χ^2 maps is consistent with the idea of grain growth in dense cores. Most regions of moderate to high extinction show up in the $R_V = 3.1$ χ^2 map but not in the $R_V = 5.5$ χ^2 map. This suggests the WD3.1 extinction law is *not* valid in extincted

regions because $\chi^2 = 4$ (the first contour level) corresponds to at least a 95% chance that the data do not fit the model. The differences in these two extinction laws is reflected by the differences in the properties of the dust models. The WD3.1 dust model was constructed to match observations of the diffuse ISM. In contrast, the WD5.5 model has significantly fewer small silicate grains ($r < 0.1\,\mu$m) and significantly more large carbonaceous ones (maximum radius $\sim 10\times$ larger).

Although most of our observations can be explained by the idea of grain growth within dense regions, both L1152 and L1228 contain regions that appear strong in the WD5.5 χ^2 map. Both of these cores have outflows associated with them which may be changing the dust sizes and compositions. In the next section, we explore changes in the observed extinction law as a function of wavelength and A_{K_s}. This will help us to understand exactly how the dust is changing within our cores.

5.2. Wavelength Dependence of the Extinction Law

As we saw in the last section, the χ^2 is strongly dependent on A_{K_s}. To explore this further, we started by binning the observed extinction law for each star into three A_{K_s} ranges: $0 < A_{K_s} \leq 0.5$, $0.5 < A_{K_s} \leq 1$, and $A_{K_s} > 1$. In each extinction bin, we combined the individual $C_{ext}^{obs}(\lambda)$ measurements to obtain a weighted average value of A_λ/A_{K_s}. As we did when computing χ^2, we again excluded any negative values of $C_{ext}^{obs}(\lambda)$.

Figure 18 shows the observed average extinction law as a function of wavelength for our cores. Each row is a different core and each column is a different range of A_{K_s}. The errorbars for each data point are the minimum uncertainty due to systematic errors in measuring flux. In addition to the WD3.1 and WD5.5 dust models, we also plot a third one, labeled KP v5.0 (Pontoppidian et al., in prep). This model is one from a grid of models constructed starting from the Weingartner & Draine (2001) parameterization of the grain size distribution. Icy mantles of water and other volatiles were then added. The specific model we use from this grid is the one with the "best fit" to the c2d mid-infrared extinction law and ice features. Several ice absorption features in this model can be seen in the figures, these are due to H_2O, CO_2, or CO.

5.2.1. The Extinction Law From 3.6 to 8 μm

From 3.6 to 8 μm, our extinction law is relatively flat for all ranges of A_{K_s} with the trend that it becomes slightly flatter as A_{K_s} increases. In Table 6 we list the average extinction

law combined over all four cores ($\beta = 1.6$). Again, the uncertainties represent the minimum error due to uncertainty in the flux. For comparison we also list the extinction law from Indebetouw et al. (2005), Flaherty et al. (2007), Lutz (1999), and our three dust models. Our data are in good agreement with other authors' results and also with the WD5.5 dust model.

Our flat extinction law for $0 < A_{K_s} \leq 0.5$ seems surprising since this result contradicts our expectation that low extinction regions should follow WD3.1, a diffuse interstellar medium dust model. In Paper I we calculated the extinction law in three molecular clouds and found that for $0 < A_{K_s} \leq 0.5$ the extinction law was consistent with WD3.1. These conflicting results may be because extinction measures the column density, not the number density, along the line-of-sight. If we assume each core has an approximate angular size of $\sim 15'$ (the lengthwise distance of any IRAC observation), and given the distances listed in Table 1, then our cores have linear sizes of $1-3\times10^5$ AU. Compare these sizes to those of the clouds in Paper I. The cloud distances in Table 1 of that paper are 125 ± 25 pc (Ophiuchus), 250 ± 50 pc (Perseus), and 260 ± 10 pc (Serpens). Assuming cloud angular sizes of $\sim 2°$, then the clouds have linear sizes of $1 - 2 \times 10^6$ AU. Finally, if we assume spherical clouds and cores, then these linear sizes also represent the depth of each cloud and core. Therefore, the number densities in our cores may be up to $10\times$ larger than in our clouds for a given column density (extinction). Grain growth is a collisional process and proceeds more rapidly at higher number densities. Hence, the grains in our isolated cores quickly achieve at least modest grain growth (represented by WD5.5 and KP v5.0) compared with the WD3.1 dust grains.

L1152 and L1155C-2 both show a strong deviation at $5.8\,\mu$m from WD5.5 for $A_{K_s} > 1$. Water ice has an absorption peak at $6.02\,\mu$m due to H-O-H bending (Gibb et al. 2004). It is possible that the high value of $A_{5.8}/A_{K_s}$ is due to the presence of water ice in these two cores, even more than predicted by the KP5.0 dust model. Mid-infrared spectra will be necessary to address this possibility.

5.2.2. The Extinction Law at 24 μm

We have only 13 stars with positive A_{24}/A_{K_s} values. These have an average value of $A_{24}/A_{K_s} = 0.59 \pm 0.12$. This value compares favorably with other empirical results. Flaherty et al. (2007) were able to measure the $24\,\mu$m extinction law for two of their five regions and found $A_{24}/A_{K_s} = 0.44 \pm 0.02$ and 0.52 ± 0.03 for Serpens and NGC 2068/71, respectively. Even though Lutz (1999) did not measure the extinction longward of $19\,\mu$m, if their flat extinction law were projected out to $24\,\mu$m, it would also have a value of ~ 0.5.

Our result also agrees with Paper I (when a model flux of 0.012 mJy at 24 μm was assumed).

Although the empirical results agree with each other, they are much higher than the 24 μm extinction law predicted by dust models. Our average value for A_{24}/A_{K_s} is $2-3\times$ larger than either the WD3.1 or WD5.5 models. The KP v5.0 dust model has a much broader 18 μm silicate peak which significantly raises the predicted 24 μm extinction. Even so, it is still too low by about 50% compared to our empirical measurement. New dust models will need to incorporate additional extinction at 24 μm.

5.2.3. Outflows in L1152 and L1228

We circled in red two regions in L1152 and L1228 (Figs. 14 and 16) with high $R_V = 5.5$ χ^2. These regions stand out because their high χ^2 values are not caused by a single star, nor are they associated with regions of high A_{K_s}. We selected all the sources within the red circles and within the $\chi^2 = 4$ contour and plotted the average extinction law for each region in Figure 19. Compared to elsewhere in the cores, the extinction law is much steeper in these two regions and more similar to the WD3.1 dust model rather than WD5.5. Because these regions are near known outflows, one possible explanation is that the outflows in each core have destroyed the bigger dust grains via shocks to produce a dust grain distribution that more closely resembles the WD3.1 diffuse ISM dust. Since neither region lines up with the outflow axis, this may be evidence for precession of the outflows, which is already observed in L1228 (Bally et al. 1995). These extinction laws could not be caused by a foreground star skewing the average because we have a total of 35 stars in the two selected regions, none with $A_{K_s} < 0.20$. A foreground star would appear to have almost zero or negative extinction, and would not greatly impact the average extinction law.

5.3. Sources of Error

5.3.1. Negative $C_{ext}(\lambda)$

In this paper we have excluded negative values for $C_{ext}(\lambda)$ as unphysical because it would imply that dust amplification, rather than extinction, is occurring. A more likely explanation is that the derived extinction or the measured flux for that wavelength is incorrect. By excluding these negative values, we introduce some potential bias into our results, which will be discussed here.

The magnitude of the bias varies with wavelength and extinction, but is much larger

at low A_{K_s}. The percentage of negative $C_{ext}(\lambda)$ values for a given wavelength ranges from $32-61\%$ for $0 < A_{K_s} \leq 0.5$, $3-17\%$ for $0.5 < A_{K_s} \leq 1$, and $0-1.8\%$ for $A_{K_s} > 1$. If we utilized these negative $C_{ext}(\lambda)$ values when computing the average extinction law, then the averages shown in Figure 18 would be $0.42-1.08\sigma$ lower for $0 < A_{K_s} \leq 0.5$, where σ is the displayed errorbar due to the minimum uncertainty in the flux. For higher extinctions, the bias is much lower because there are far fewer negative $C_{ext}(\lambda)$ values. The average extinction law decreases $0.05-0.52\sigma$ for $0.5 < A_{K_s} \leq 1$ and for $A_{Ks} > 1$, the decrease is $0-0.06\sigma$.

The large bias we find for $0 < A_{K_s} \leq 0.5$ suggests that our technique for computing the extinction law breaks down at low extinctions. We discussed this before in relation to Figure 17. We have not attempted to incorporate any bias from excluding the negative $C_{ext}(\lambda)$ into our errorbars since the bias is partially due to the fluxes, and we already set a lower limit on the errors due to our minimum uncertainty in measuring the fluxes at different wavelengths. However, our results presented in this paper may slightly overestimate the mid-infrared extinction law, primarily for $A_{K_s} \leq 0.5$.

5.3.2. Changes in the Near-Infrared Extinction Law

Many authors have fit the near-infrared extinction to a power law, $A_\lambda \propto \lambda^{-\beta}$, with $\beta = 1.6-1.8$ (Draine 2003, and references therein). The WD3.1 and WD5.5 models are very similar in the near-infrared JHK_s bands, reflecting this apparent universality of the near-infrared extinction law. These two models both have $\beta \approx 1.6$. This law does agree with the apparent reddening vector in our data (see Figure 5) and makes our results directly comparable with other authors' results who have made the same assumption. However, it is possible that the extinction law could be steeper in some regions. This would introduce another source of error into our calculated extinction law. To calculate the magnitude of this effect, we modified the WD5.5 dust model to have $\beta = 1.8$ in the JHK_s bands and used this law instead of the WD5.5 model for classifying sources and computing the extinctions and the extinction law. Our results can be seen in Table 6 and Figure 20. As stated before, the uncertainties in our average extinction law are the minimum errors due to uncertainty in the flux.

Using a $\beta = 1.8$ law slightly decreases our mid-infrared extinction law, however the qualitative results of this paper are unchanged. Even with $\beta = 1.8$ our extinction law is more consistent with WD5.5 for all ranges of extinction. The biggest difference is for $A_{K_s} > 1$ in L1152 and L1155C-2. With $\beta = 1.8$, the excess $A_{5.8}/A_{K_s}$ extinction disappears. We argued in § 5.2.1 that this excess could possibly be explained by the existence of water

ice in these two cores. The circled regions in our χ^2 figures that may be caused by outflows destroying the big dust grains appear even stronger with our $\beta = 1.8$ law. This is because the difference from WD5.5 is enhanced.

6. Conclusions

In this paper we presented deep JHK_s and *Spitzer* photometry of four isolated cores: L204C-2, L1152, L1155C-2, and L1228. Based on previous observations, two of these cores were classified as starred and two were classified as starless. Our data support these original classifications. We detect 10 YSOs, three within L1152, seven within L1228, and none within L204C-2 or L1155C-2. Seven of these YSOS have not been previously discovered. Among these, we are able to resolve the driving source of the HH200 outflow in L1228 into two sources separated by $5\farcs3$, but we were unable to identify which of the two sources is responsible for the outflow.

To put constraints on possible faint YSOs in all four cores, we selected 634 sources with 24 μm detections $\geq 3\sigma$ which are either undetected or too faint at other wavelengths to be considered in our high reliability catalogs. We computed the median SED for these sources and integrated the SED to obtain a luminosity of 7×10^{-5} to 5×10^{-4} $L_\odot$ with colors of a very young Flat spectrum or Class I YSO (Greene et al. 1994).

In addition to studying the YSO content of these cores, we used the line-of-sight measurements of the extinction and the extinction law to create maps of the extinction and χ^2 deviation from specific dust grain models. Our extinction law is nearly flat for all ranges of extinction in all four cores. In the IRAC bands ($3.6 - 8\,\mu$m) this extinction law matches the predictions of the WD5.5 dust model, a model designed to simulate the grain growth that occurs in dense regions, and also agrees with the other authors' results (Indebetouw et al. 2005; Flaherty et al. 2007; Lutz 1999). In the densest regions of L1152 and L1155C-2, the 5.8 μm extinction law is higher than the WD5.5 model. This could be evidence for water ice in these cores or a steeper near-infrared extinction law than the average value. At 24 μm, our data are consistent with the extinction law remaining constant as the total extinction increases. The observed extinction law is much higher than that predicted by dust grain models, but does confirm the similarly large value found by other authors (Chapman et al. 2009; Flaherty et al. 2007; Lutz 1999).

From the χ^2 maps we identified cavities in L1152 and L1228 where the extinction law is more consistent with the WD3.1 dust model. The molecular outflows in these cores produce shocks, which may be destroying the large dust grains, thus producing a dust distribution

similar to WD3.1 These cavities are visible in our χ^2 maps, but would be missed in averages over an entire core.

It is critical to create new dust grain models which reproduce the observed flat extinction law, especially at 24μm. In this paper we used the Robitaille et al. (2007) models to estimate the luminosities of our YSOs. However, Robitaille et al. (2007) assumed an extinction law that is between WD3.1 and WD5.5 in the IRAC bands and predicts a 24 μm extinction that is about 25% of our observed value. The best-fit YSO parameters would undoubtedly change with a flatter extinction law. Furthermore, it is important to understand the mid-infrared extinction law because future telescopes, such as the James Webb Space Telescope, will operate at these wavelengths.

We are grateful to Neal Evans for providing useful feedback on several drafts and also the anonymous referee whose comments greatly improved the quality of this paper. Support for this work, utilizing data from the "Cores to Disks" Spitzer Legacy Science Program (Evans et al. 2003), was provided by NASA through contracts 1224608, 1230782, and 1230779 issued by the Jet Propulsion Laboratory, California Institute of Technology, under NASA contract 1407. Additional support for N.L.C. was provided by NASA through JPL contracts 1264793 and 1264492. L.G.M. was supported by NASA Origins Grant NAG510611. This research has made use of PyRAF, a product of the Space Telescope Science Institute, which is operated by AURA for NASA. We also used the SIMBAD database which is operated at CDS, Strasbourg, France.

REFERENCES

Bally, J., Devine, D., Fesen, R. A., & Lane, A. P. 1995, ApJ, 454, 345

Chapman, N. L., Mundy, L. G., Lai, S.-P., & Evans, II, N. J. 2009, ApJ, in press

de Geus, E. J., de Zeeuw, P. T., & Lub, J. 1989, A&A, 216, 44

Draine, B. T. 2003, ARA&A, 41, 241

Elston, R. 1998, in Proc. SPIE Vol. 3354, p. 404-413, Infrared Astronomical Instrumentation, Albert M. Fowler; Ed., ed. A. M. Fowler, 404–413

Evans, II, N. J., et al. 2003, PASP, 115, 965

Flaherty, K. M., Pipher, J. L., Megeath, S. T., Winston, E. M., Gutermuth, R. A., Muzerolle, J., Allen, L. E., & Fazio, G. G. 2007, ApJ, 663, 1069

Foster, J. B., Román-Zúñiga, C., Goodman, A. A., Lada, E., & Alves, J. 2008, ApJ, 674, 831

Gibb, E. L., Whittet, D. C. B., Boogert, A. C. A., & Tielens, A. G. G. M. 2004, ApJS, 151, 35

Greene, T. P., Wilking, B. A., Andre, P., Young, E. T., & Lada, C. J. 1994, ApJ, 434, 614

Haikala, L. K., & Laureijs, R. J. 1989, A&A, 223, 287

Harvey, P. M., et al. 2007, ApJ, 663, 1149

Indebetouw, R., et al. 2005, ApJ, 619, 931

Jarrett, T. H. 1992, PhD thesis, AA(Massachusetts Univ., Amherst.)

Jarrett, T. H., Dickman, R. L., & Herbst, W. 1994, ApJ, 424, 852

Koornneef, J. 1983, A&A, 128, 84

Kun, M. 1998, ApJS, 115, 59

Lombardi, M., & Alves, J. 2001, A&A, 377, 1023

Lutz, D. 1999, The Universe as Seen by ISO, 427, 623

Makovoz, D., & Marleau, F. R. 2005, PASP, 117, 1113

Press, W. H., Teukolsky, S. A., Vetterling, W. T., & Flannery, B. P. 1992, Numerical Recipies in C, The Art of Scientific Computing (Cambridge, MA: Cambridge Univ. Press)

Robitaille, T. P., Whitney, B. A., Indebetouw, R., & Wood, K. 2007, ApJS, 169, 328

Schechter, P. L., Mateo, M., & Saha, A. 1993, PASP, 105, 1342

Shu, F. H., Adams, F. C., & Lizano, S. 1987, ARA&A, 25, 23

Straizys, V., Cernis, K., Kazlauskas, A., & Meistas, E. 1992, Baltic Astronomy, 1, 149

Surace, J. A., et al. 2004, VizieR Online Data Catalog, 2255, 0

Weingartner, J. C., & Draine, B. T. 2001, ApJ, 548, 296

A. Average Stellar Models

To compute the expected stellar distribution for each core, we used the galaxy model from Jarrett (1992) and Jarrett et al. (1994). Given the Galactic coordinates, distance, and average extinction for a core, this model produces source counts broken down by spectral type. These source counts provide a rudimentary weighting function that can be used in computing the average stellar model. However, a weighting function from the raw source counts ignores the reality that not all spectral types are equally observable at each wavelength. Our next step was to correct for the detection limits of our actual observations. The galaxy model lists the extincted K_s magnitude for each star and its extinction, A_V. We used this information, the Weingartner & Draine (2001) $R_V = 3.1$ extinction law, and the stellar templates from the SSC's "star-pet"[4] tool to compute the magnitude of each star at every observed waveband from J to 24 μm. We then arbitrarily discarded any detection falling below the 5σ cutoff for the given waveband (Table 3). Lastly, we used the normalized, final, corrected source counts at each waveband as a weighting function, and computed the overall average stellar model. We repeated this procedure using both the Weingartner & Draine (2001) $R_V = 5.5$ extinction law and also using the magnitude limits from our deeper JHK_s observations. Both variables have a negligible effect on the final fluxes.

After these calculations, we made one final adjustment to our average stellar model. In Paper I we determined that the above method produces a 24 μm flux that is very likely too high. However, we can independently put an upper-limit on the 24 μm flux value. If we select all stars with line-of-sight $0 < A_{K_s} \leq 0.5$ and compute the average 24 μm to K_s flux ratio, this will give us an estimate of the true average 24 μm stellar flux. Since these stars have small amounts of extinction, this ratio will over-estimate the true value because the K_s band is more extincted than 24 μm. There are 28 stars in our cores with 24 μm fluxes $\geq 3\sigma$ and within the extinction range $0 < A_{K_s} \leq 0.5$. These have an average 24 μm to K_s flux of 0.013 ± 0.001 with an average extinction of 0.19 A_{K_s}. This is the same as the value derived using the Galaxy count models. Given the non-zero average extinction, the true flux ratio will be lower. Therefore, in this paper we will assume it is actually 0.012. Our final average stellar flux for the JHK_s, IRAC1-4, and MIPS1 bands, respectively, is: 1.282 ± 0.144, 1.302 ± 0.050, 1., 0.453 ± 0.010, 0.268 ± 0.005, 0.179 ± 0.005, 0.102 ± 0.003, and 0.012 ± 0.001. Note that all fluxes are scaled relative to the K_s band.

[4] `http://ssc.spitzer.caltech.edu/tools/starpet`

Table 1. Basic Properties of the Cores

Core	l (deg.)	b (deg.)	Dist. (pc)
L204C-2	6	20	125 ± 25[a]
L1152	102	16	325 ± 25[b]
L1155C-2	102	15	325 ± 25[b]
L1228	111	20	200 ± 50[c]

[a]de Geus et al. (1989)

[b]Straizys et al. (1992)

[c]Kun (1998)

Table 2. Summary of *Spitzer* Observations

Core	AOR Number	Date Observed YYYY-MM-DD	Program ID
L204C-2	11393792	2005-04-07	3656
	11396352	2005-04-08	3656
	11392000	2005-08-22	3656
	11398912	2005-08-23	3656
L1152	11390976	2004-07-23	3656
	11399424	2004-07-28	3656
	11394304	2004-10-15	3656
	11396864	2004-11-10	3656
L1155C-2	11392768	2004-07-22	3656
	11399936	2004-08-12	3656
	11394816	2004-12-02	3656
	11397376	2004-12-26	3656
L1228	11391232	2004-11-28	3656
	11395072	2004-12-07	3656
	11400192	2004-12-16	3656
	11397632	2004-12-26	3656

Table 3. Sensitivity Limits

Band	Central λ (μm)	10 σ (mag.)	5 σ (mag.)
J	1.235	19.5(19.9)	20.3(20.7)
H	1.662	18.8(19.7)	19.5(20.4)
K_s	2.159	17.7(18.6)	18.4(19.3)
IRAC1	3.550	18.6	19.7
IRAC2	4.493	17.8	18.8
IRAC3	5.731	15.5	16.4
IRAC4	7.872	14.7	15.6
MIPS1	23.7	10.4	11.7

Note. — The parenthetical values are the limits obtained for our deeper observations towards the dense core regions L1152 and L1155C-2.

Table 4. Photometry of Young Stellar Objects

Index	Core	RA (J2000)	DEC (J2000)	J (mJy)	H (mJy)	K_s (mJy)	3.6 μm (mJy)	4.5 μm (mJy)	5.8 μm (mJy)	8.0 μm (mJy)	24 μm (mJy)	70 μm (mJy)
1	L1152	20 35 46.3	67 53 02.2	0.130	0.696	1.57	3.59	6.44	5.50	3.36	280	3670
2	L1152	20 36 11.6	67 57 09.3	9.19	25.5	36.1	41.3	47.9	60.8	77.8	183	347
3	L1152	20 36 19.9	67 56 31.6	52.8	130.	205	228	243	259	262	597	1080
4	L1228	20 55 37.1	77 38 19.6	5.76	7.18	7.21	5.69	4.68	3.78	3.89	4.58	···
5	L1228	20 57 06.8	77 36 56.1	0.541	1.78	3.13	7.81	11.1	13.9	18.5	271	2240
6	L1228	20 57 08.0	77 36 59.7	0.624	1.91	2.82	3.16	3.46	3.28	7.32	154	···
7	L1228	20 57 13.0	77 35 43.3	8.74	58.5	143	262	374	499	762	2680	7850
8	L1228	20 57 15.5	77 34 23.6	0.141	0.715	1.79	2.00	2.41	2.46	2.94	5.04	···
9	L1228	20 57 17.0	77 36 58.6	5.14	15.1	26.1	31.3	38.0	37.2	42.1	83.8	334
10	L1228	20 58 40.0	77 27 45.5	1.17	3.08	6.53	22.9	···	24.7	···	43.6	···

Table 5. Selected Model YSO Parameters

Source ID	Envelope Accretion Rate (10^{-6} $M_\odot$/year)	Disk Mass 10^{-6} $M_\odot$	Interstellar A_V (mag)	L_{bol} ($L_\odot$)	YSO Class[a]
1	$0.05 - 26.15$ (10.18)	$10 - 11,000$ (1,600)	$4.7 - 15.6$ (10.6)	$0.52 - 3.17$ (1.19)	I
2	$0 - 0.10$ (0.05)	$230 - 5,300$ (2,800)	$4.0 - 10.8$ (7.4)	$2.06 - 2.68$ (2.37)	II
3	$0 - 0.16$ (0.07)	$590 - 85,000$ (14,000)	$6.5 - 10.5$ (8.9)	$7.61 - 21.25$ (11.18)	II
4	$0 - 0$ (0)	$3.6 - 18$ (11)	$1.5 - 1.8$ (1.7)	$0.03 - 0.03$ (0.03)	II
5	$0.21 - 4.38$ (2.36)	$14 - 760$ (420)	$3.4 - 12.9$ (7.1)	$0.35 - 3.21$ (0.93)	I
6	$0 - 7.15$ (0.32)	$3.4 - 12,000$ (880)	$2.8 - 12.7$ (10.7)	$0.04 - 3.31$ (0.20)	I
7	$0 - 0.11$ (0.07)	$8,900 - 26,000$ (20,000)	$16.5 - 16.8$ (16.6)	$9.63 - 12.57$ (10.61)	Flat
8	$0 - 0$ (0)	$0.55 - 860$ (89)	$11.9 - 16.4$ (15.0)	$0.03 - 0.15$ (0.04)	II
9	$0.13 - 0.13$ (0.13)	$15 - 15$ (15)	$9.4 - 10.3$ (9.8)	$0.29 - 0.29$ (0.29)	II
10	$0 - 19.07$ (4.99)	$8.3 - 58,000$ (4,600)	$0.1 - 12.3$ (4.8)	$0.24 - 5.19$ (0.96)	Flat

[a]Greene et al. (1994)

Note. — The parenthetical values denote the average value for each quantity

Table 6. Average Relative Extinction A_λ/A_{K_s}

Source	3.6 μm	4.5 μm	5.8 μm	8 μm	24 μm
All cores, $\beta = 1.6$	0.64 ± 0.07	0.49 ± 0.06	0.48 ± 0.06	0.47 ± 0.05	0.59 ± 0.12
All cores, $\beta = 1.8$	0.57 ± 0.08	0.40 ± 0.07	0.40 ± 0.06	0.37 ± 0.05	0.47 ± 0.06
Flaherty et al. (2007)	0.632 ± 0.004	0.54 ± 0.01	0.50 ± 0.02	0.50 ± 0.01	0.46 ± 0.04
Indebetouw et al. (2005)	0.56 ± 0.06	0.43 ± 0.08	0.43 ± 0.10	0.43 ± 0.10	$\cdots$
Lutz (1999)[a]	0.53 ± 0.03	0.50 ± 0.08	0.49 ± 0.06	0.42 ± 0.06	$\cdots$
WD3.1[b]	0.40	0.25	0.17	0.22	0.17
WD3.1[b]	0.60	0.49	0.40	0.41	0.24
KP, v5.0[b]	0.48	0.38	0.34	0.38	0.38

[a]The extinction for the closest ISO wavelength to each *Spitzer* band is listed: 3.7, 4.4, 5.9, and 7.5 μm

[b]Extinctions for dust models are computed at the central wavelength in each band

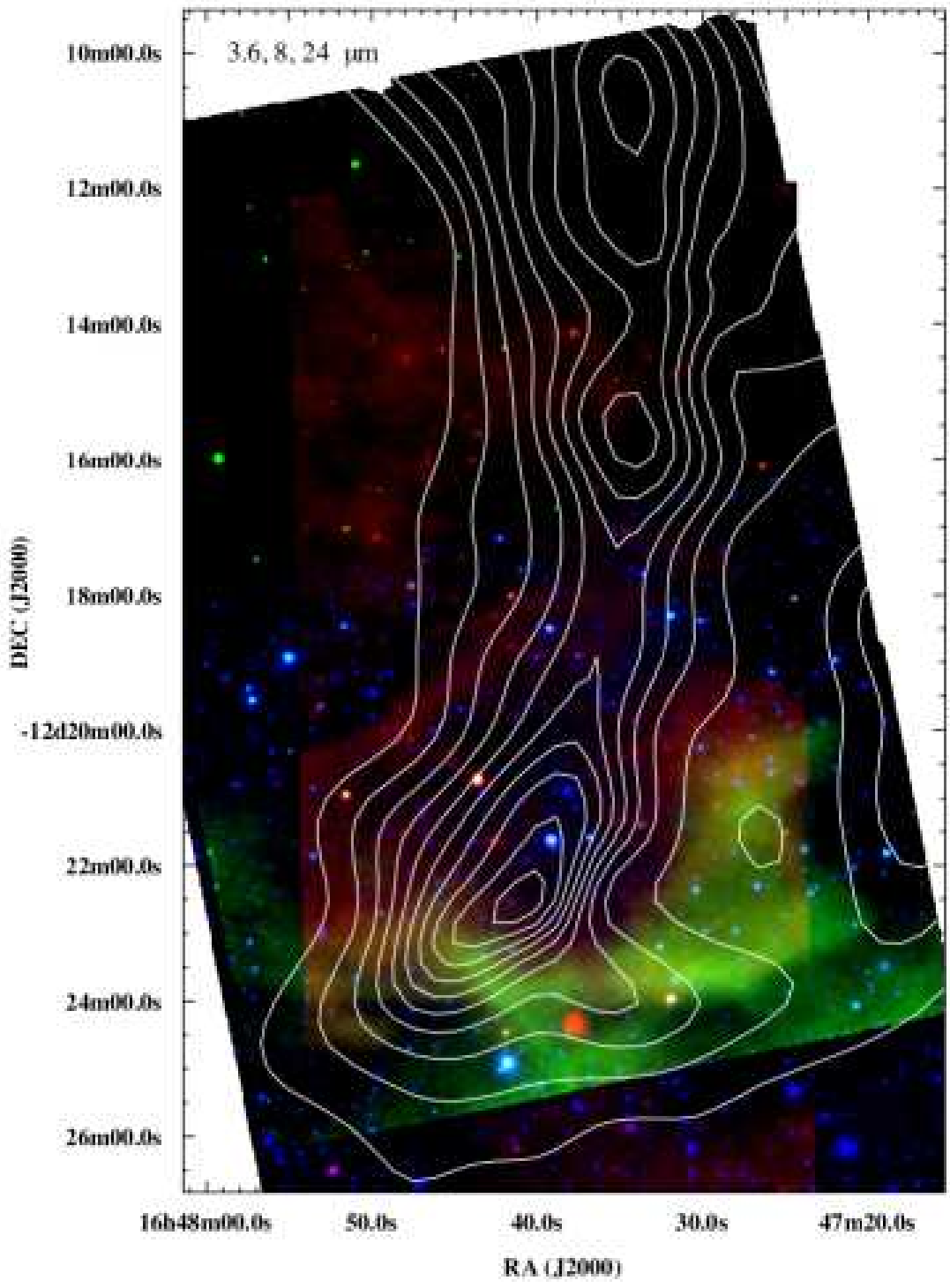

Fig. 1.— Three-color image of L204C-2. The contours are from the extinction map (§ 3). The 24, 8, and 3.6 μm channels are used for the red, green, and blue emission, respectively.

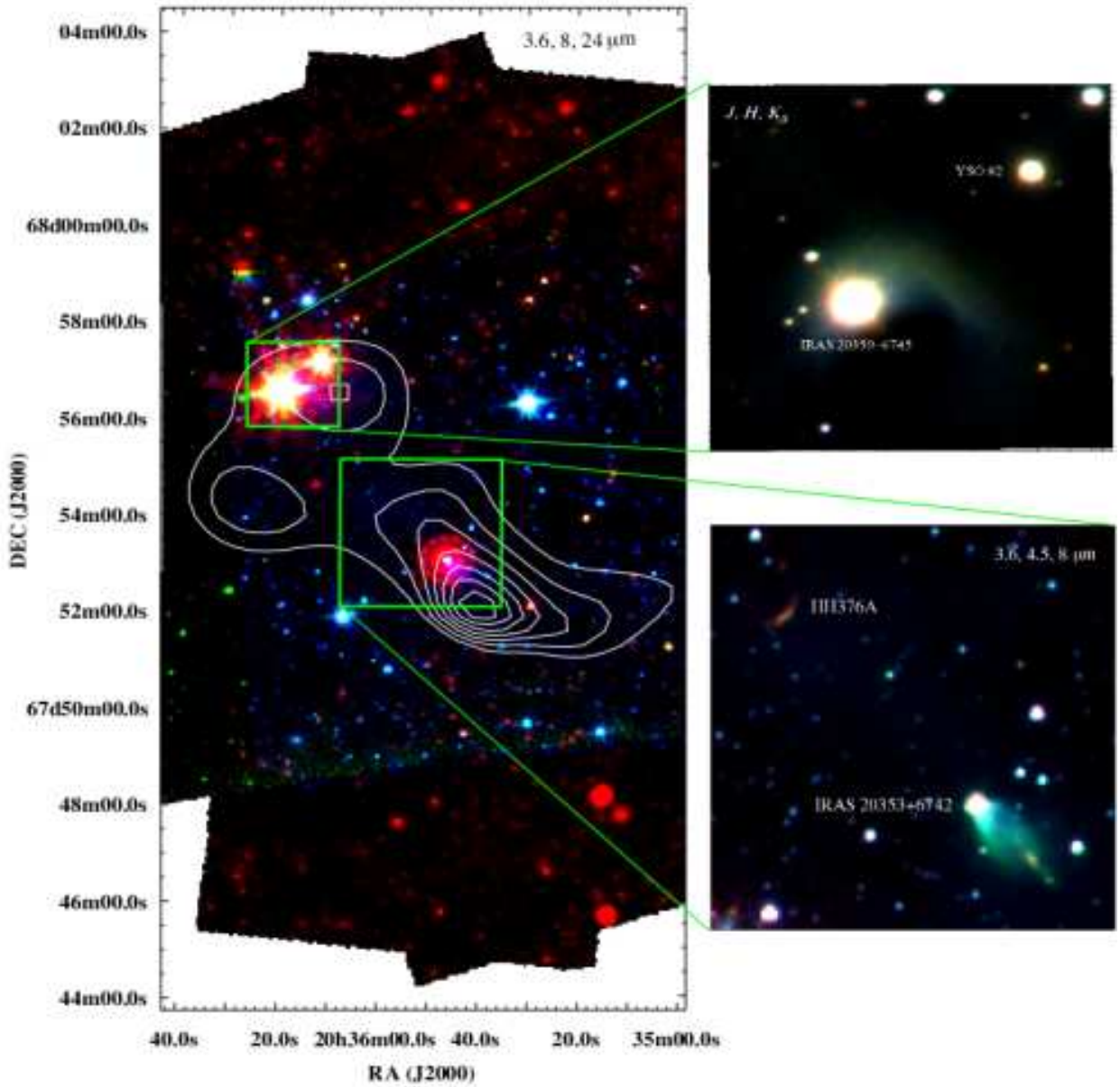

Fig. 2.— Three-color image of L1152. The contours are from the extinction map (§ 3). The wavelengths used for the blue, green, and red emission, respectively, are listed at the top of each sub-figure.

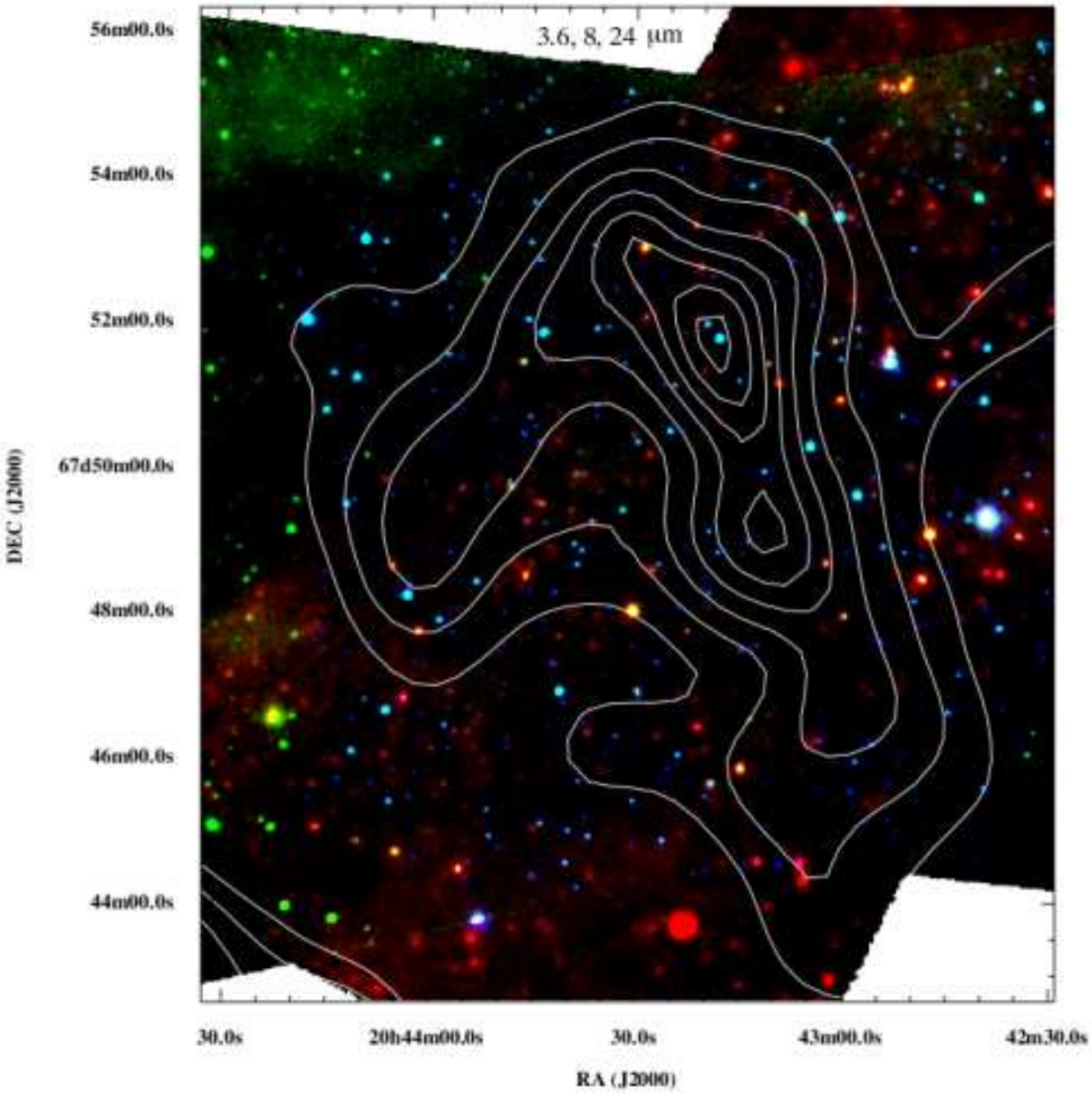

Fig. 3.— Three-color image of L1155C-2. The contours are from the extinction map (§ 3). The 24, 8, and 3.6 μm channels are used for the red, green, and blue emission, respectively.

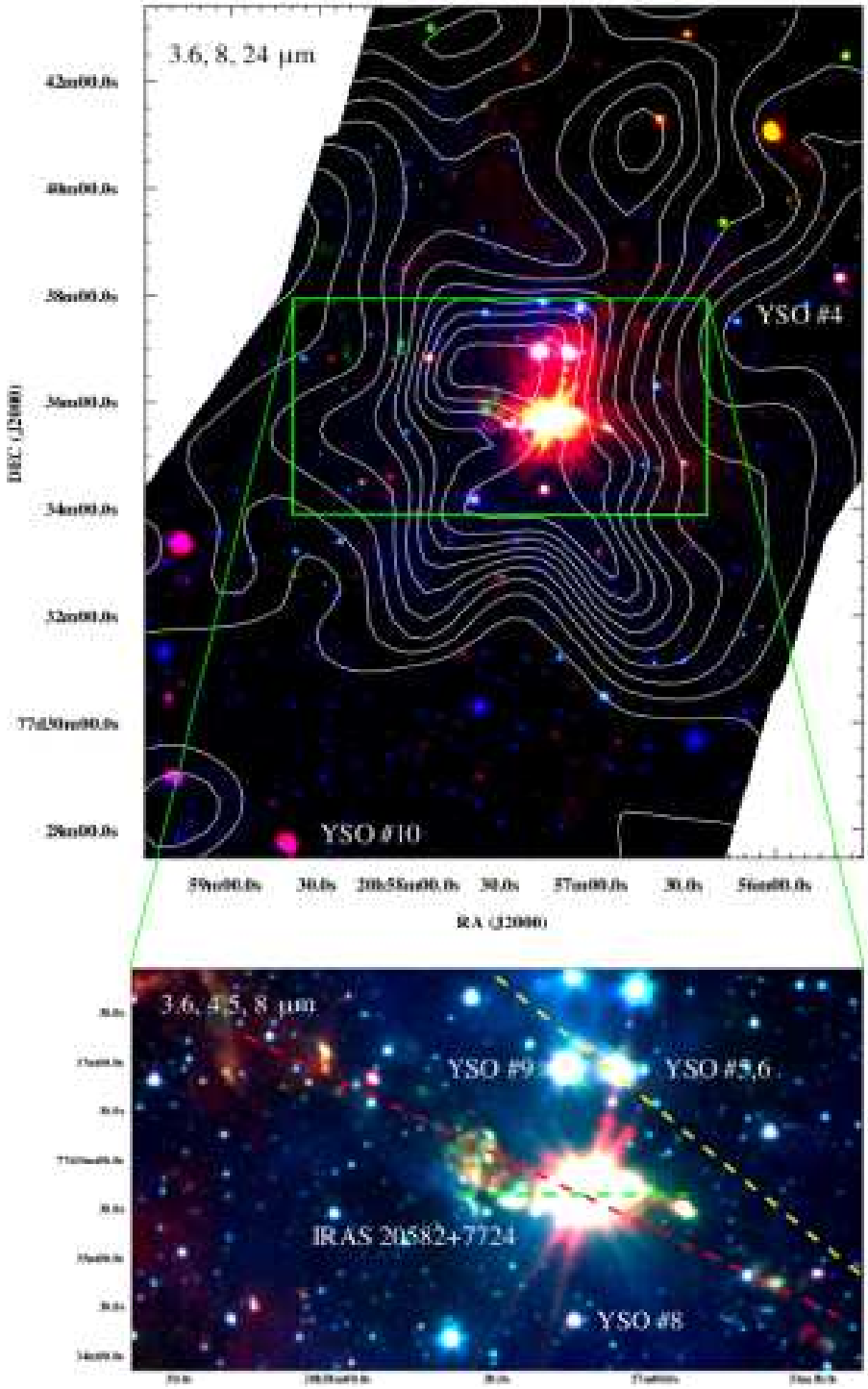

Fig. 4.— Three-color image of L1228. The contours are from the extinction map (§ 3). The wavelengths used for the blue, green, and red emission, respectively, are listed at the top of each sub-figure.

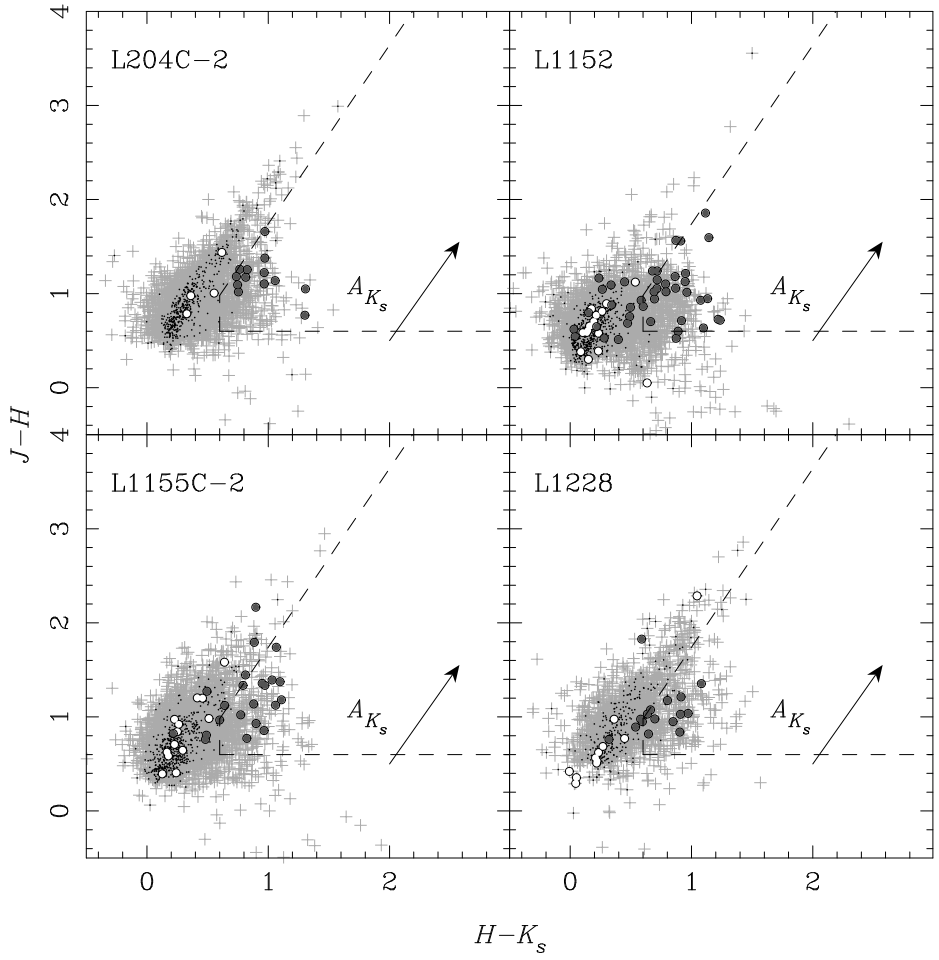

Fig. 5.— $J - H$ vs. $H - K_s$ color-color diagram of the high-reliability stars for each core. The gray crosses are all the stars, while the black points are those stars brighter than 15th magnitude at K_s. Overlaid on the stars are white and dark gray circles, which are the 'known' stars and background galaxies, respectively. These sources were selected from Figure 6. The reddening vector for our extinction law, WD5.5, is also shown. See § 2.5 for a description of the dashed lines and further details.

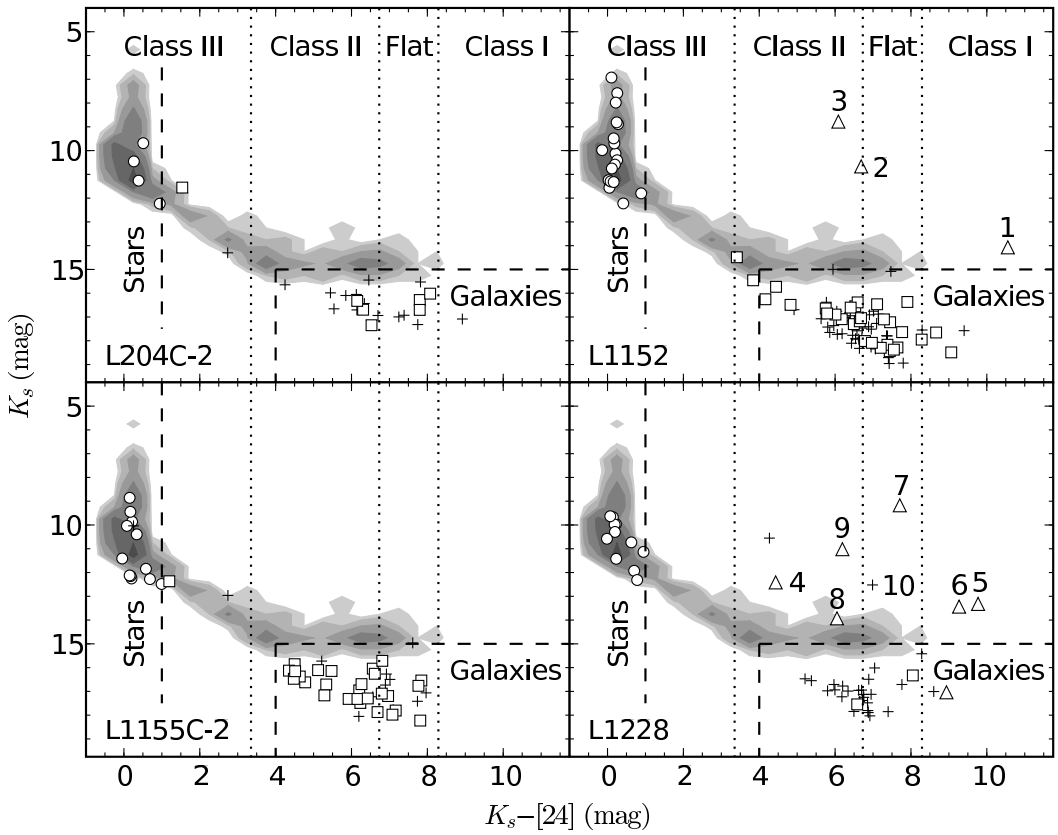

Fig. 6.— K_s vs. $K_s - [24]$ plot of all sources with JHK_s detections $\geq 7\sigma$ and 24 μm $\geq 3\sigma$. We used four different symbols to correspond to different source classifications: stars are circles, Galc sources are squares, YSOc objects are triangles, and plus signs denote all other classifications. The shaded contours are from the c2d processed catalog of part of ELAIS N1 (Surace et al. 2004). The dashed lines denote the cutoffs we used for selecting 'known' stars and background galaxies, while the dotted lines are the cutoffs for different YSO evolutionary classes as defined by Greene et al. (1994). The YSOs discussed in this paper are numbered for easy reference.

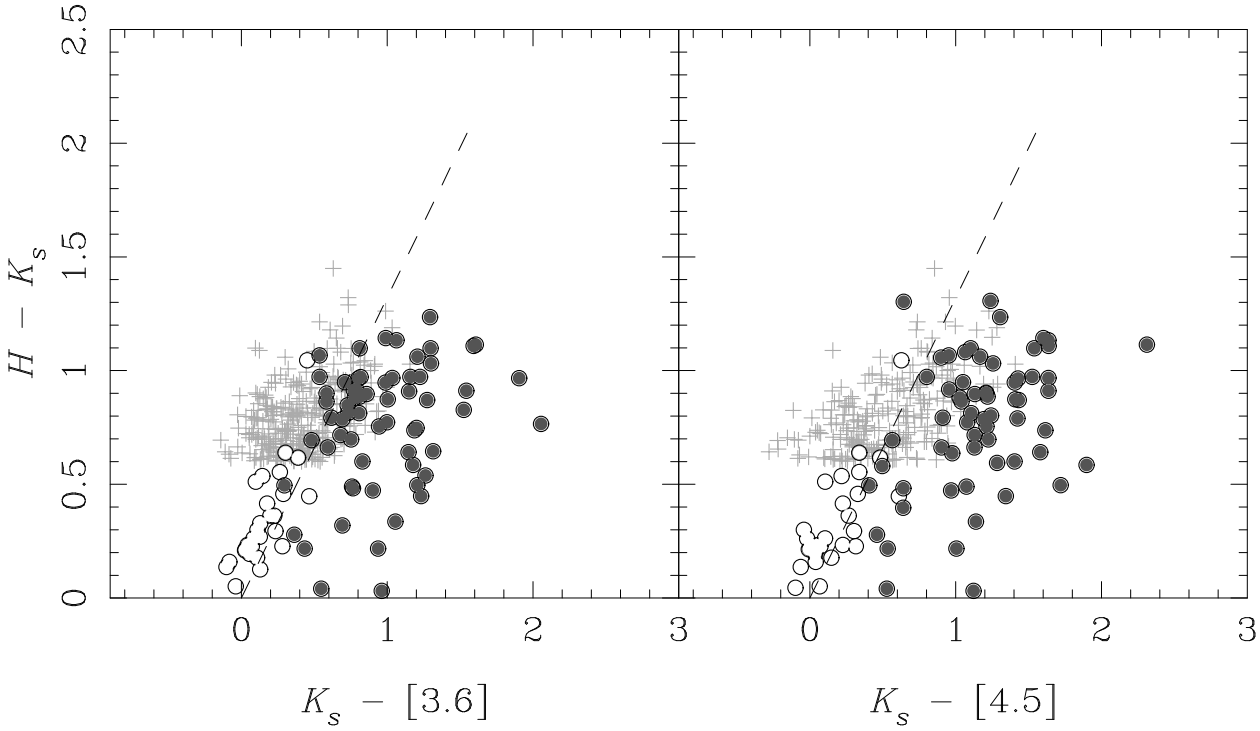

Fig. 7.— $H - K_s$ vs. $K_s - [3.6]$ (left) and vs. $K_s - [4.5]$ (right). The gray crosses are the sources selected by the dashed lines in Figure 5 while the white and dark gray circles are the 'known' stars and background galaxies, respectively. The dashed line in each panel has the equation $H - K_s = 1.32x$ where x is either $K_s - [3.6]$ or $K_s - [4.5]$.

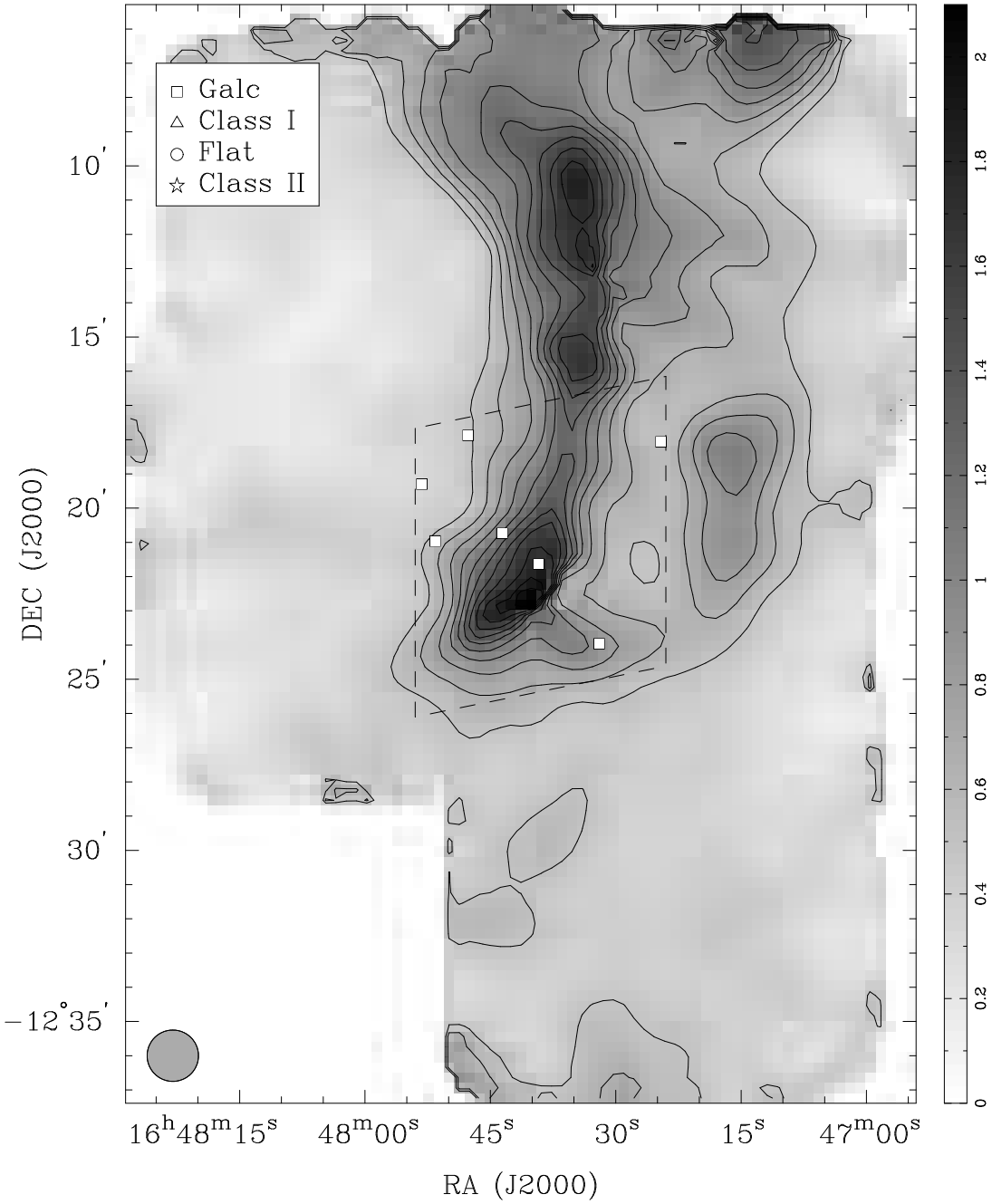

Fig. 8.— Extinction map of L204C-2. The map has a resolution of 90″ with a maximum A_{K_s} value of 2.1 magnitudes. The contours start at $A_{K_s} = 0.5$ mag. in steps of 0.15 (3σ). Sources classified as Galc are shown as squares, while YSOs are shown with one of three symbols, depending on their evolutionary classification (Greene et al. 1994). There are no YSOs plotted in this figure. The dashed region denotes the approximate area covered with both IRAC and MIPS. The gray circle denotes the resolution of the map.

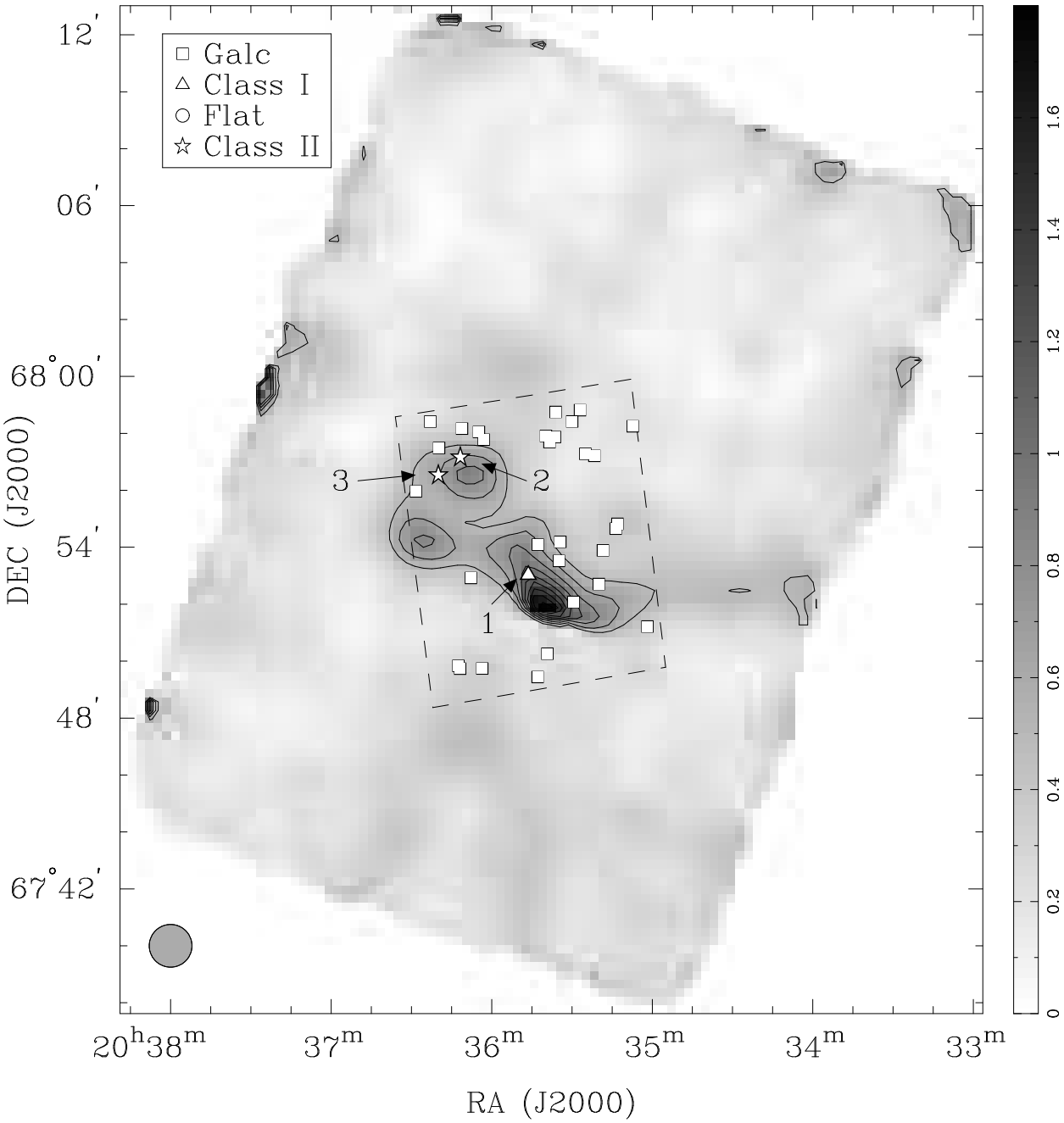

Fig. 9.— Extinction map of L1152. The maximum A_{K_s} value in the map is 1.8 magnitudes. See Figure 8 for a description of the contours, symbols, and dashed lines. The numbered sources are the YSOs discussed in § 4.

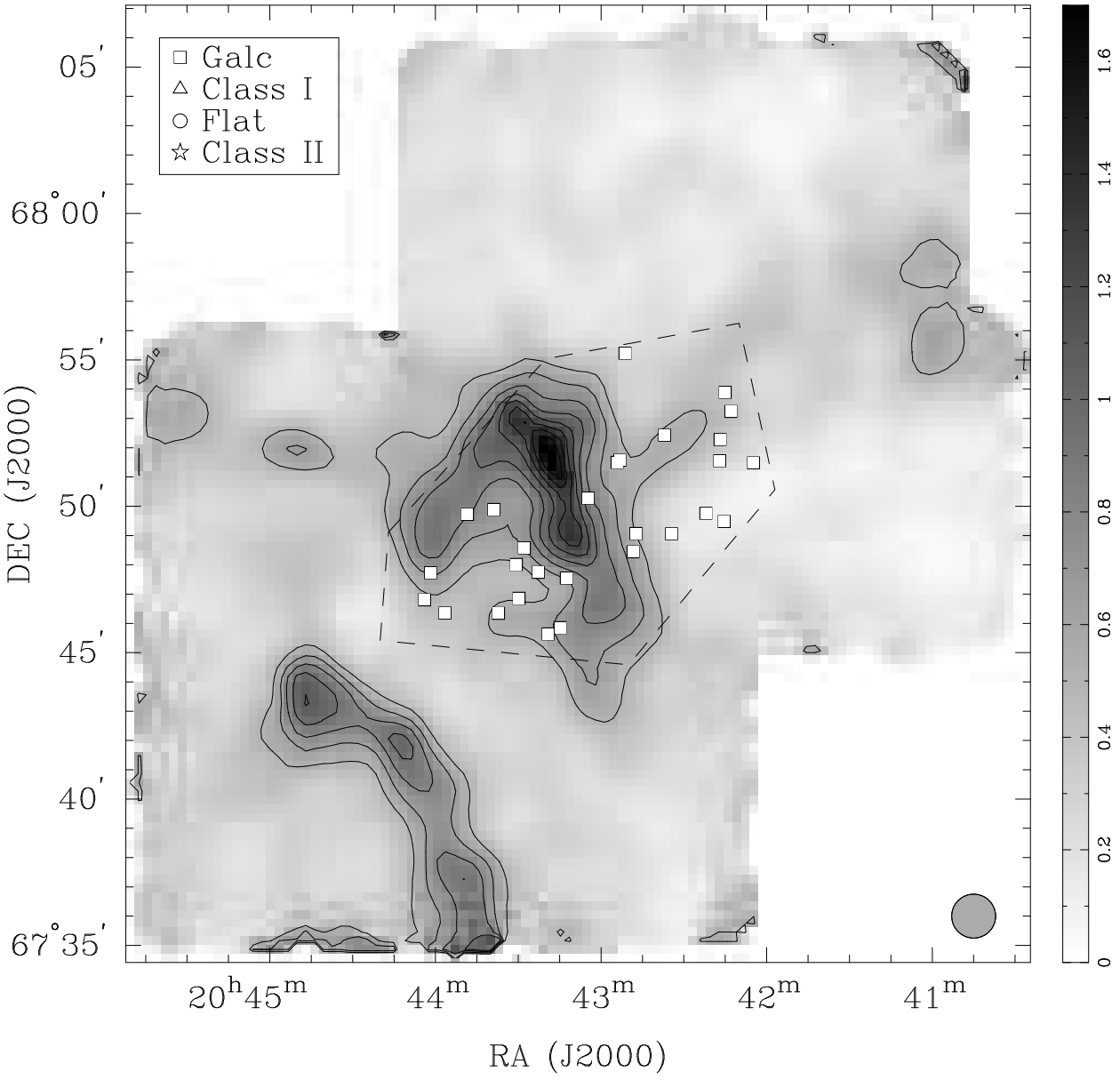

Fig. 10.— Extinction map of L1155C-2. The maximum A_{K_s} value in the map is 1.7 magnitudes. See Figure 8 for a description of the contours, symbols, and dashed lines. There are no YSOs plotted in this figure.

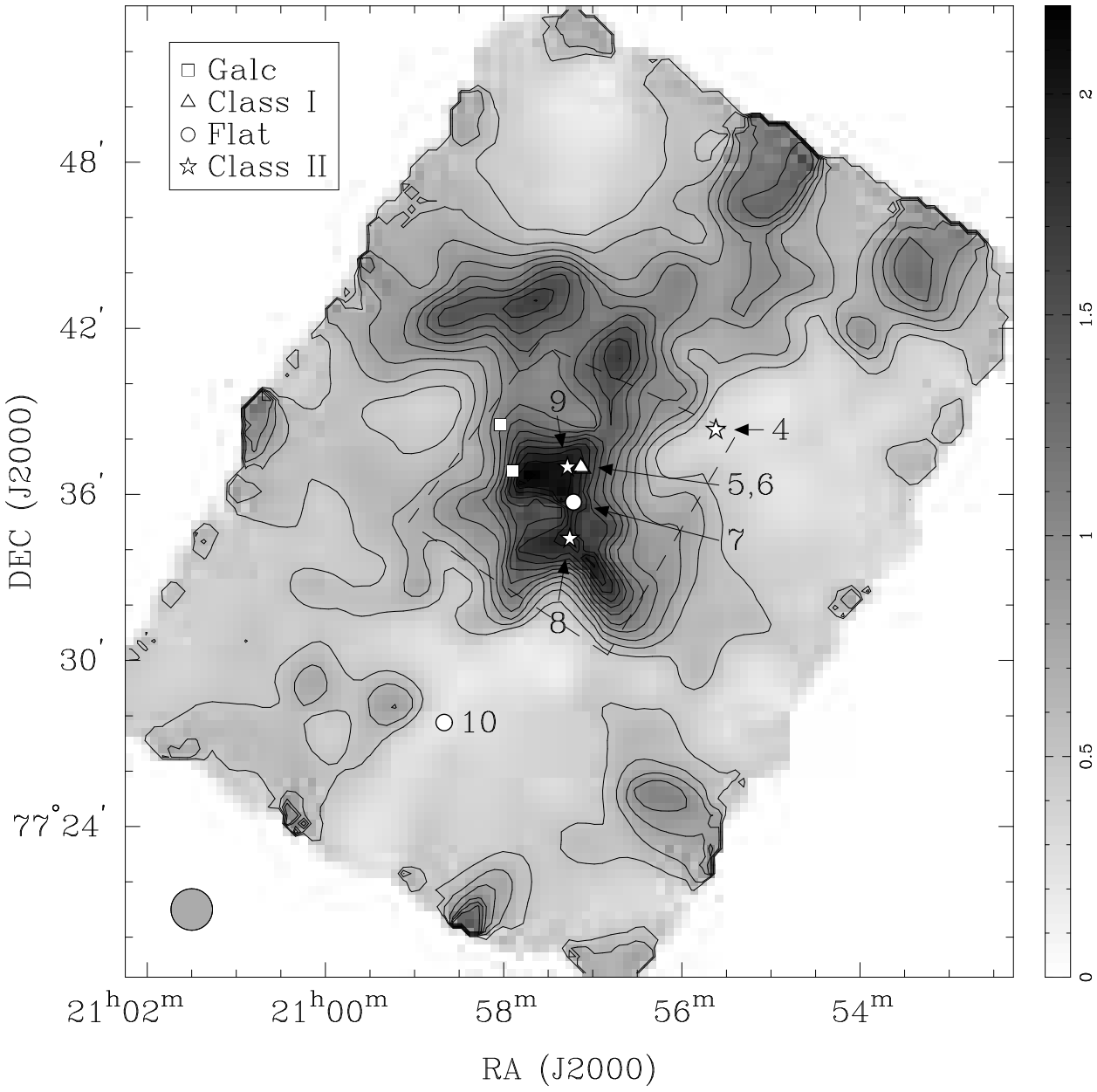

Fig. 11.— Extinction map of L1228. The maximum A_{K_s} value in the map is 2.2 magnitudes. See Figure 8 for a description of the contours, symbols, and dashed lines. The numbered sources are the YSOs discussed in § 4.

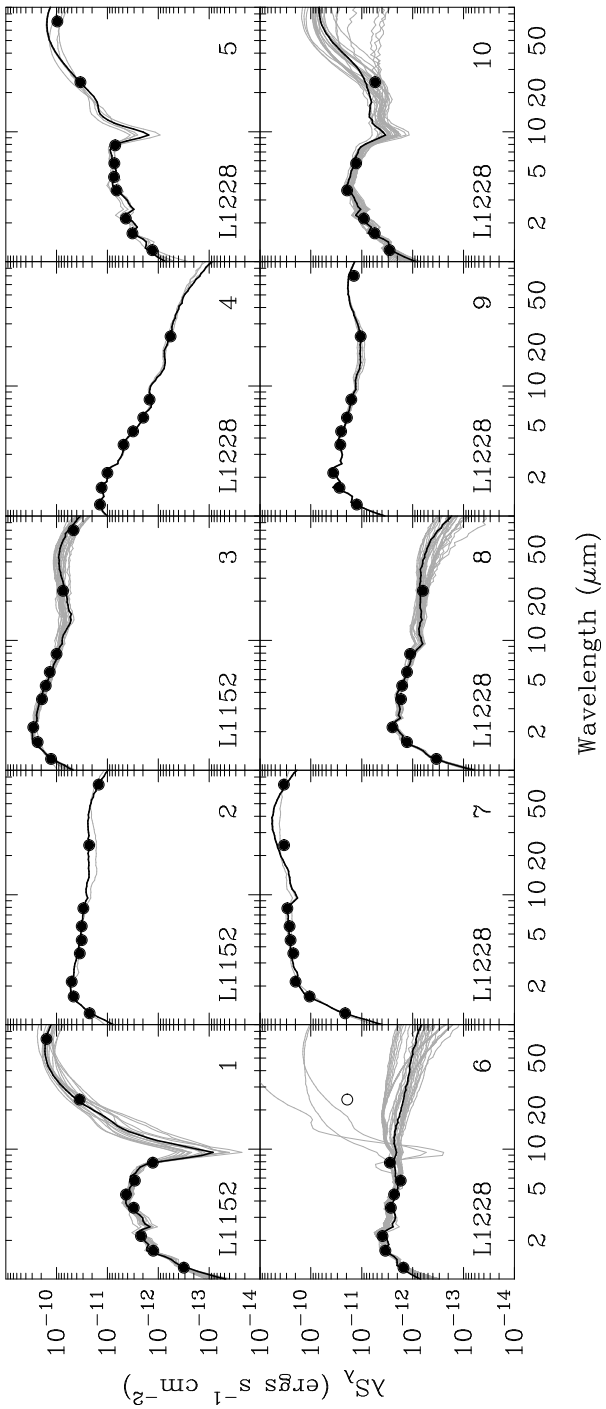

Fig. 12.— The spectral energy distributions for our 10 YSOs. The black curve is the best-fit YSO model from Robitaille et al. (2007) while the gray curves show other model fits with $\chi^2 \leq 2 \times \chi^2_{best}$ (§ 4). The errorbars are smaller than the datapoints. Each YSO is numbered for reference.

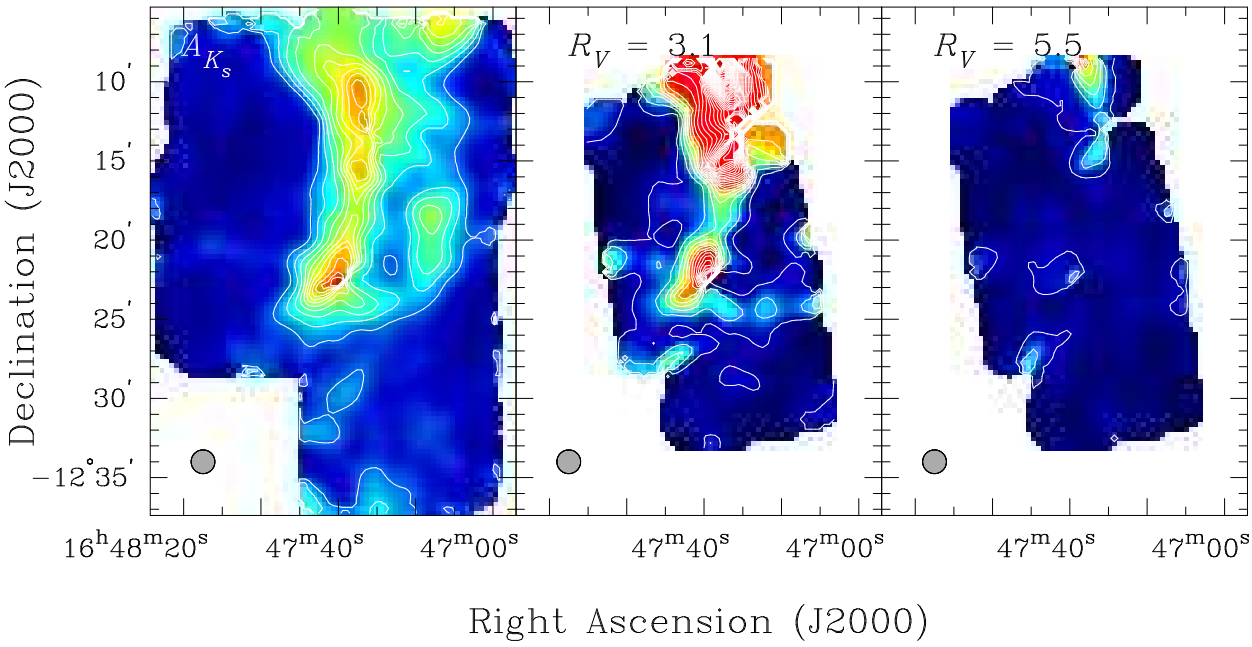

Fig. 13.— Map of the χ^2 values in L204C-2. The left panel shows the A_{K_s} map with contours starting at 0.5 magnitudes in steps of 0.15 mag. (3σ). The middle and right panels show χ^2 using either the Weingartner & Draine $R_V = 3.1$ (middle) or $R_V = 5.5$ (right) dust models with contours starting at 4 in steps of 4. The gray circle in the lower left corner denotes the resolution of the maps, 90″.

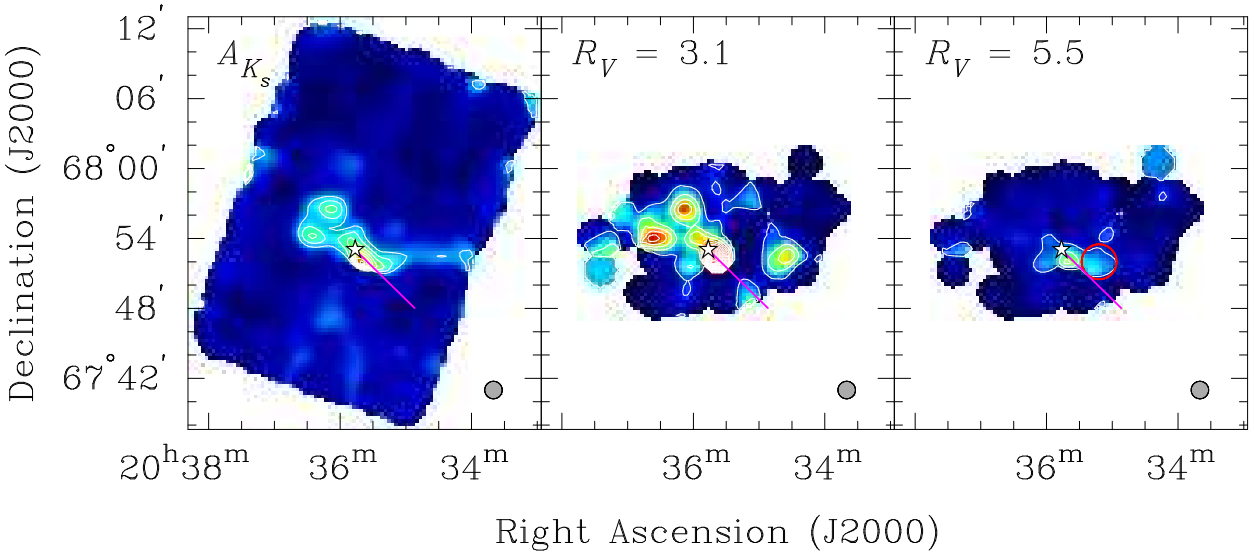

Fig. 14.— Same as Figure 13 except for L1152. The star denotes the position of YSO #1 and the magenta line shows the direction of the outflow axis. See § 5.2.3 for a discussion of the red circle in the $R_V = 5.5$ panel.

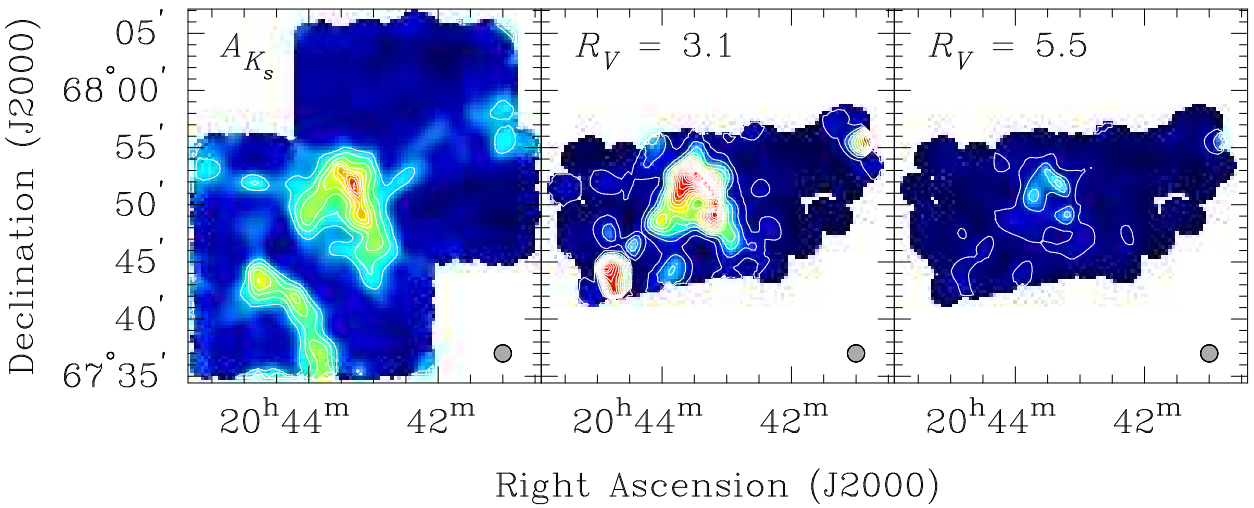

Fig. 15.— Same as Figure 13 except for L1155C-2.

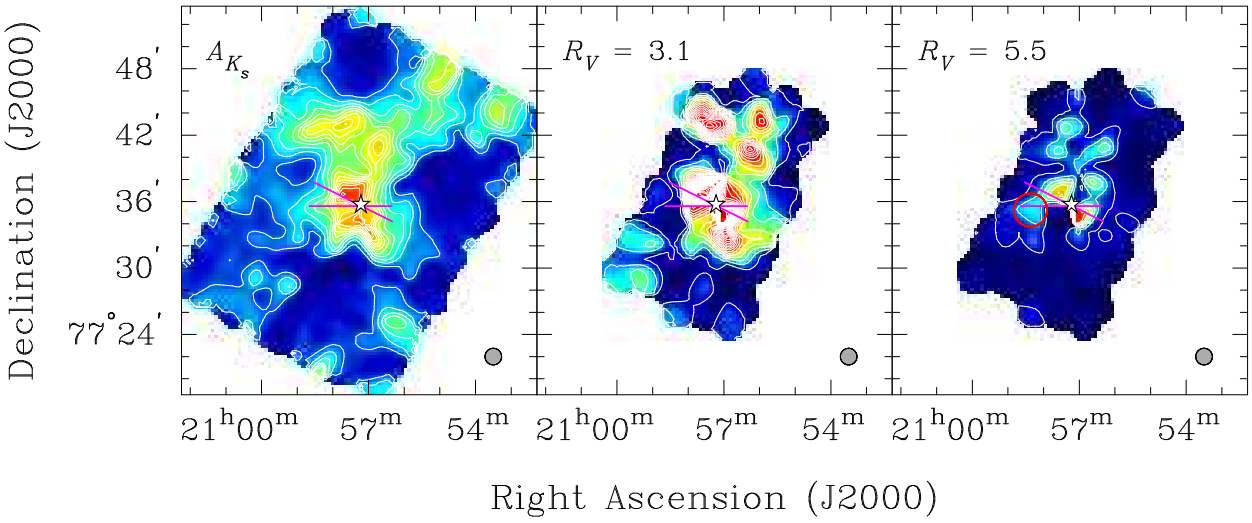

Fig. 16.— Same as Figure 13 except for L1228. The star denotes the position of YSO #7 and the magenta lines show the directions of the outflow axes. See § 5.2.3 for a discussion of the red circle in the $R_V = 5.5$ panel.

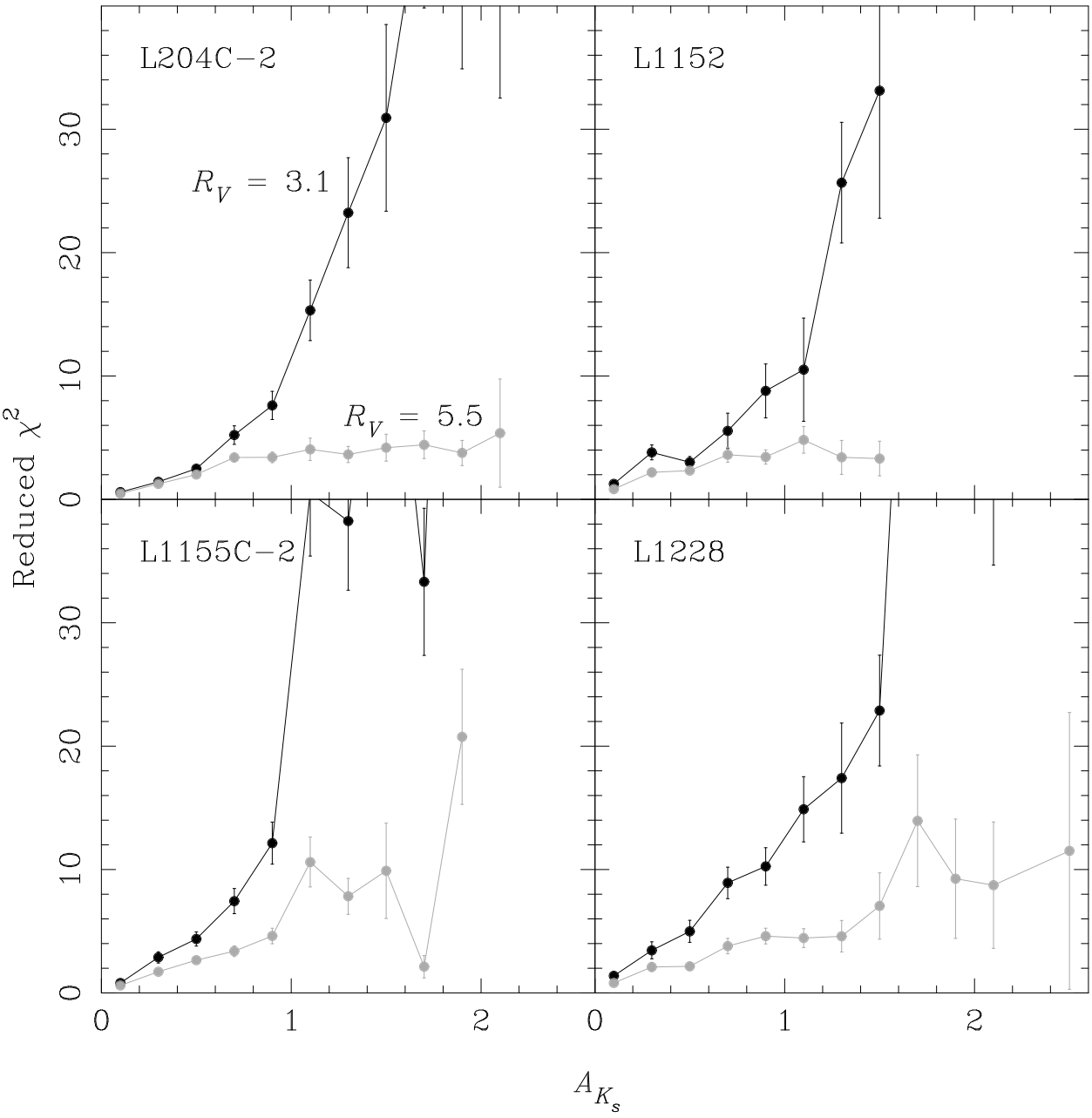

Fig. 17.— χ^2 versus A_{K_s} for our cores. The WD3.1 χ^2 values are black; the WD5.5 χ^2 values are light gray. The error bars shown are the standard deviations of the mean in each bin.

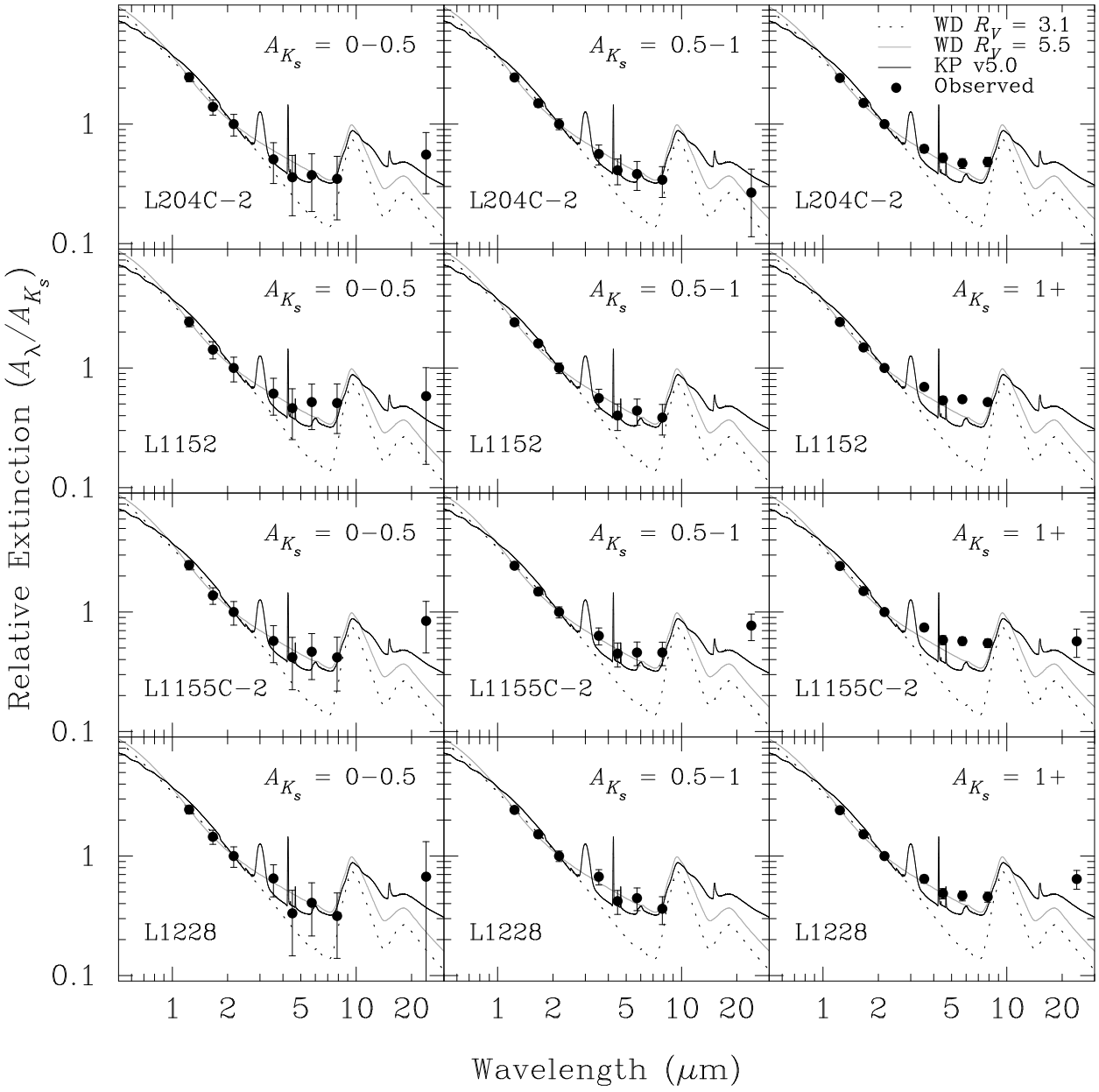

Fig. 18.— The extinction law for each core divided into three A_{K_s} ranges. Extinctions were computed using the WD5.5 dust model with $\beta = 1.6$ in the JHK_s bands. The left column is sources with $0 < A_{K_s} \leq 0.5$, the middle column is $0.5 < A_{K_s} \leq 1$, and the right column is $A_{K_s} > 1$. The errorbars represent the minimum uncertainty in measuring the fluxes.

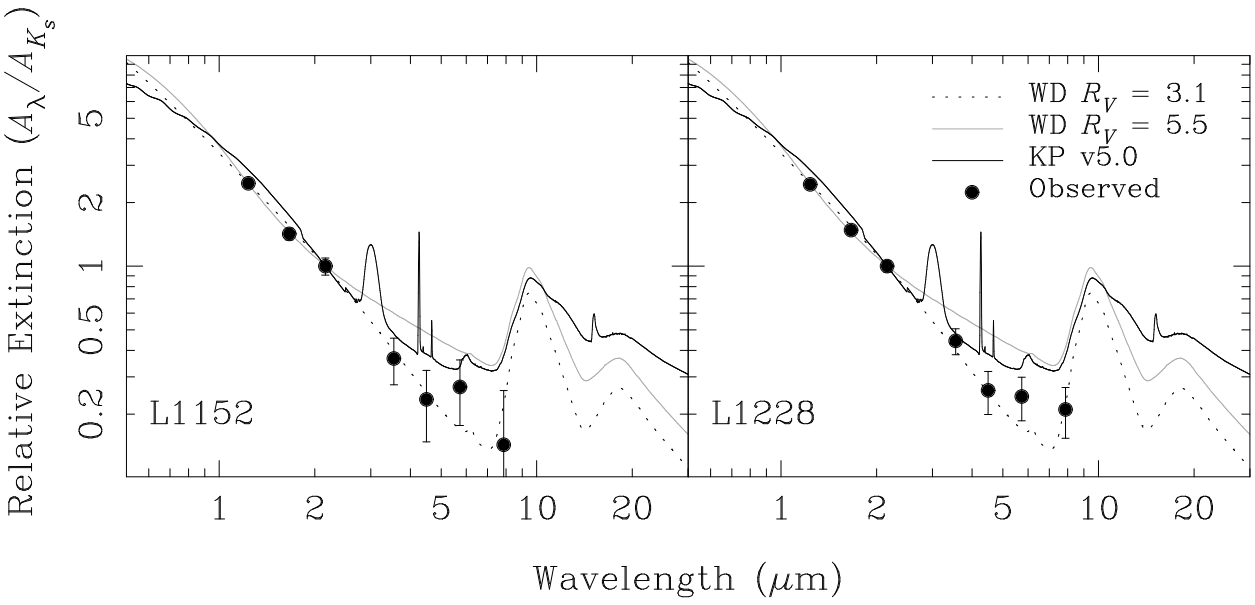

Fig. 19.— The averaged extinction laws for the sources near the outflows in L1152 (left) and L1228 (right). Three different dust models are plotted for comparison. The errorbars are the minimum uncertainty due to the systematic errors in the flux.

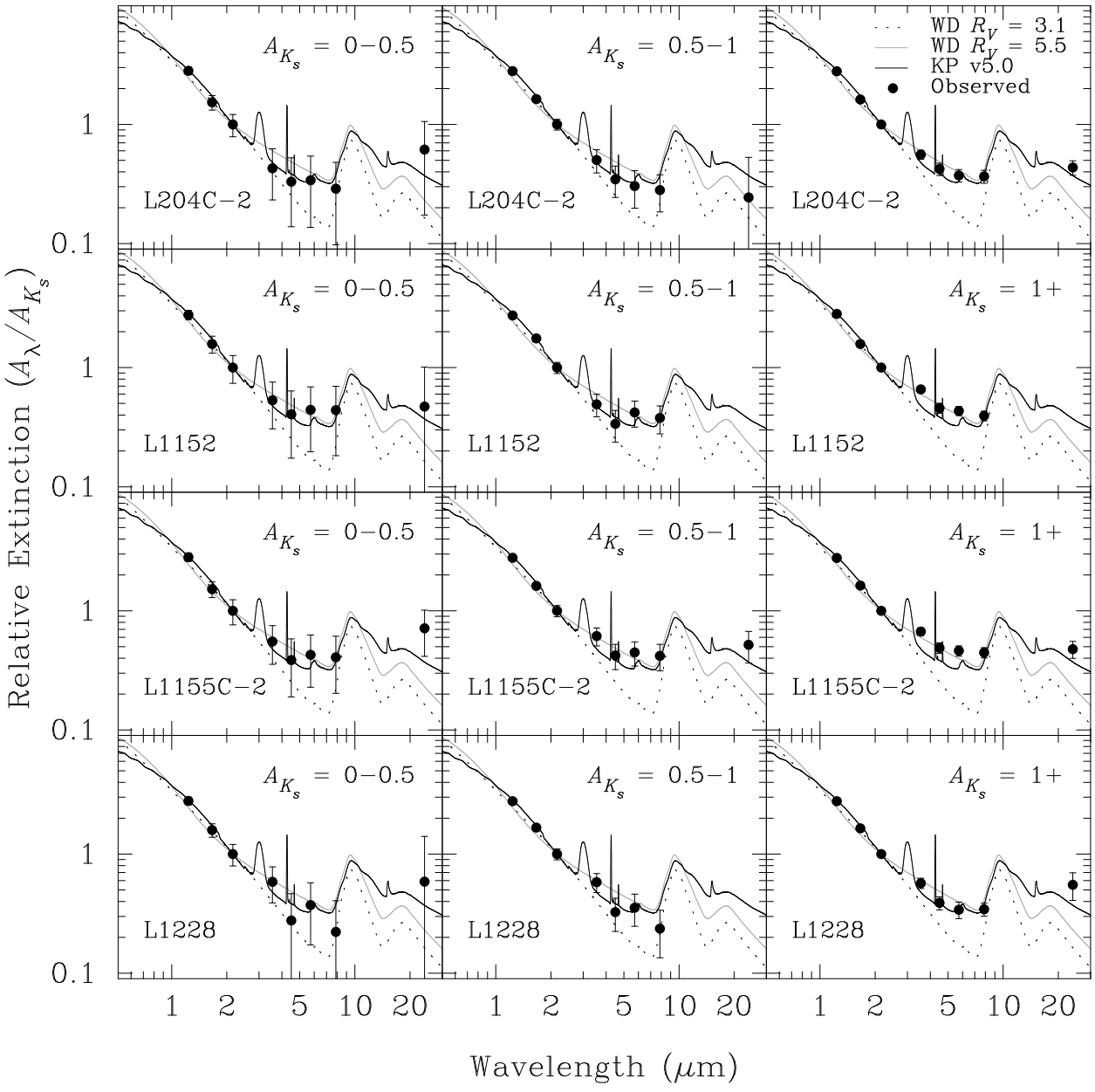

Fig. 20.— Same as Figure 18 except using an extinction law with $\beta = 1.8$ in the JHK_s bands for computing extinctions and source classification.